Investigation of the reaction ^{144}Sm(p, p') under extreme forward angles

Untersuchung der Reaktion ^{144}Sm(p, p') unter extremen Vorwärtswinkeln

Bachelor-Thesis by Dirk Martin

October 2011

TECHNISCHE UNIVERSITÄT DARMSTADT

Fachbereich Physik
Institut für Kernphysik

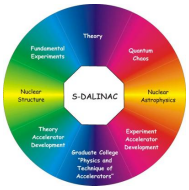

Supported by the DFG through SFB 634 and NE 679/3-1.

Investigation of the reaction ^{144}Sm(p, p') under extreme forward angles
Untersuchung der Reaktion ^{144}Sm(p, p') unter extremen Vorwärtswinkeln

vorgelegte Bachelor-Thesis von Dirk Martin

1. Gutachten: Prof. Dr. P. von Neumann-Cosel
2. Gutachten: Dr. I. Poltoratska

Tag der Einreichung:

Zusammenfassung

Im Rahmen dieser Bachelor-Thesis werden Daten zur (p, p') Streuung am stabilen, halbmagischen Kern ^{144}Sm untersucht. Das Experiment wurde mit hoher Energieauflösung unter 0° bei einer Energie von 295 MeV am Research Center for Nuclear Physics (RCNP) in Osaka, Japan, im Mai 2011 aufgenommen.
Das Ziel des Experiments ist die Extraktion der B(E1) und B(M1) Stärkeverteilungen sowie die Erforschung des Einflusses der Deformation auf diese Stärkeverteilung im Vergleich mit Messungen am wohldeformierten Kern ^{154}Sm. Die Analyse der Daten umfasst die Korrektur von Winkel- und Impulsinformationen der gestreuten Protonen mithilfe der in Vieldrahtkammern gemessenen Driftzeiten. Es wurden differentielle Wirkungsquerschnitte der Spektren im Winkelbereich von 0° – 4° bestimmt. Die Vergleiche mit Rechnungen zur Coulombanregung in Eikonalnäherung bestätigen den E1-Charakter des Wirkungsquerschnitts im Bereich der Dipolriesenresonanz. Außerdem wird ein qualitativer Vergleich mit Daten aus ^{144}Sm(γ, γ') Experimenten angestellt, welche im Jahr 2001 am supraleitenden Darmstädter Elektronenlinearbeschleuniger S-DALINAC durchgeführt wurden.

Abstract

In the framework of this bachelor thesis results from a (p, p') scattering experiment on the stable, semi-magical nucleus ^{144}Sm are studied. The data were obtained in high-resolution experiments with a proton beam energy of 295 MeV under 0° at the Research Center for Nuclear Physics (RCNP) Osaka, Japan, in May 2011.

The aims of this experiment are the extraction of the B(E1) and B(M1) strength distributions as well as the investigation of the influence of the deformation on these strength distributions in comparison with measurements on the well-deformed nucleus ^{154}Sm. The data analysis involves the extraction of angle and momentum information for the scattered protons from the measured drift times, measured in multi-wire drift chambers. Differential cross sections of the spectra are determined for angles between 0° and 4°. By comparison to theoretical predictions of Coulomb excitation using the eikonal approximation, the E1 character of the cross sections in the region of the GDR can be confirmed. Furthermore, a qualitative comparison to data obtained in ^{144}Sm(γ, γ') experiments at the superconducting Darmstadt electron linear accelerator in the year 2001 is drawn.

Contents

List of Figures

List of Tables

1 Introduction

The study of electric and magnetic resonances permits the investigation of collective phenomena in many-body fermionic quantum systems. The excitations can be characterized due to their angular momentum (ΔL), spin (ΔS) and isospin (ΔT) transfer. Recently the study of the electric dipole response has been an important issue of nuclear structure research. The electric dipole excitations in spherical nuclei can be divided into three different types, which are shown in Fig. 1.1: The giant dipole resonance (GDR), the pygmy dipole resonance (PDR) and the low-lying two-phonon state.

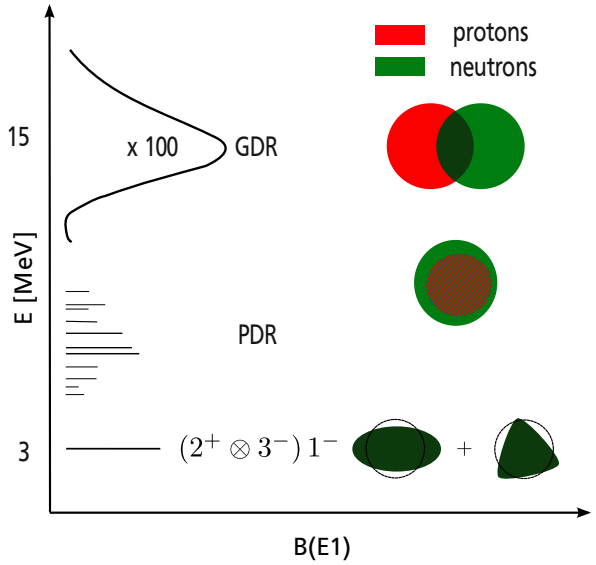

Figure 1.1: Schematic view of the electric dipole excitations in nuclei in the energy range from 3–20 MeV.

Exhausting the major part of the electric dipole strength the GDR is located in an excitation energy region between 10 MeV and 20 MeV. It can be illustrated as a collective oscillation of all neutrons against all protons. The centroid energy of this typical broad structure can be approximated [1] by a function depending on the mass number A

$$E_x = 31.2\ \text{MeV} \cdot A^{-1/3} + 20.6\ \text{MeV} \cdot A^{-1/6}. \tag{1.1}$$

At low excitation energies a two-phonon state is observed, which results from the $[2^+ \otimes 3^-]_{1-}$ coupling [2] and describes low-energy collective surface vibrations of the nucleus. Between the two-phonon state and the GDR, the PDR is situated. This kind of resonance is supposed to arise from oscillations of the neutron excess against a stable proton-neutron core with $N \simeq Z$. The PDR has been known for a long time [3], however the characteristics and systematics are

poorly understood. It is assumed that the induced dipole moments and the summed transition strengths depend on the neutron excess. Consequently, the total transition strength should increase with the number of excess neutrons in neutron-rich nuclei. Thus, investigation of the PDR are of high interest for understanding nuclear structure, but also for astrophysics, where it may influence neutron-capture rates in the r-process nucleosythesis involving nuclei with very large neutron excess [4].

A common method to study the PDR is nuclear resonance fluorescence (NRF). Low-lying E1 strength and its fine structure has been explored by experiments at $Z = 20$ [5], $Z = 50$ [6], $Z = 82$ [9] and $N = 82$ [8] shell closures performed at the S-DALINAC in Darmstadt. The $N = 50$ shell closure [7] was investigated at the ELBE photon-scattering facility in Dresden-Rossendorf. Although high resolutions are achieved in these experiments, this technique is limited, because the measured cross sections depend on the ground-state decay branching ratios, which are unknown and typically estimated to be 100%. In addition to this, the PDR can only be observed up to the particle separation threshold and hence its strength may not be captured completely.

Another method, which is not affected by the restrictions of NRF, is (p, p') scattering at extreme forward angles [10]. It enables measurements over the whole excitation energy region of the PDR and the GDR and might allow to distinguish between different theoretical predictions. Several high-resolution experiments of this type have already been performed successfully at the Research Center of Nuclear Physics (RCNP) in Osaka, Japan. Using polarized proton beams with an energy of about 300 MeV the complete electric and magnetic spin dipole response of ^{12}C was extracted [11] introducing polarization transfer observables. Furthermore it was shown that this method is in good agreement with a multipole decomposition procedure for ^{208}Pb [12]. In the latter work also the fine structure of the GDR was examined via wavelet transforms leading to a better understanding of the damping mechanisms of giant resonances in heavy nuclei. Additionally, analyses of experiments regarding the spherical nucleus ^{120}Sn [13, 14] and the heavy deformed nucleus ^{154}Sm are underway [15].

In this work the (p, p') reaction on the semi-magic nucleus ^{144}Sm at the $N = 82$ shell closure, measured at the RCNP, is analyzed. The nucleus ^{144}Sm is of utmost importance in nuclear astrophysics to clarify p-process abundances. For this reason the dipole strength in ^{144}Sm has recently been studied via (γ, n), (γ, p) and (γ, α) reactions [16]. Besides, it serves as a benchmark for the study of ^{154}Sm, where the impact of the deformation on the PDR and the spin-M1 resonance is investigated.

This thesis is structured in the following way. First an introduction to the theoretical background of proton scattering and Coulomb excitation is given in chapter 2. The experimental setup for high resolution measurements is described in chapter 3. Thereafter chapter 4 presents the main steps in the data analysis and the obtained results including a comparison to (γ, γ') data. Finally the thesis concludes with a summary and outlook in chapter 5.

2 Theoretical background

2.1 Inelastic proton scattering

In inelastic proton scattering at very small momentum transfers two kinds of interactions occur. A distinction is made between the excitations caused by the nuclear force, e.g. spinflip excitations, and electromagnetic excitations. The former excitations can be described using an effective nucleon-nucleus interaction, whereas electromagnetic excitations are dominant at very forward angles and can be described by the Coulomb interaction of dipole transitions. If the energy of the projectile is below the Coulomb barrier

$$U_{Coulomb} = \frac{1}{4\pi\varepsilon_0}\frac{Z_1 Z_2 e^2}{r}, \tag{2.1}$$

only Coulomb excitation will take place. In Eq. (2.1), ε_0 is the electric constant, r is the interaction radius and Z_1, Z_2 are the atomic numbers of projectile and target, respectively. For higher energies both interactions contribute coherently to the scattering cross section.

2.2 Nucleon-nucleus scattering

Nuclear structure has been studied extensively via nucleon-nucleus scattering in the intermediate energy region (100 MeV $\leq E_0 \leq$ 500 MeV) [11]. In this energy region single-step processes are dominant and distortion effects are very small. Thus the distorted-wave impulse approximation (DWIA), in which the potential energy of the target nucleus is neglected, provides a good description of inelastic proton scattering. Here, the distortion of incoming and outgoing waves is characterized by optical potentials. As protons possess spin $S = 1/2$ and isospin $T = 1/2$ the following excitation modes are permitted

- isoscalar non-spinflip ($\Delta T = 0$, $\Delta S = 0$),
- isoscalar spinflip ($\Delta T = 0$, $\Delta S = 1$),
- isovector non-spinflip ($\Delta T = 1$, $\Delta S = 0$),
- isovector spinflip ($\Delta T = 1$, $\Delta S = 1$).

Based on the phenomenological free nucleon-nucleon (NN) scattering amplitudes, Franey and Love [17] derived a projectile-nucleus interaction for beam energies of 100-800 MeV

$$V(\vec{r},\vec{p}) = V^C(r) + V^{LS}(r)\vec{L}\cdot\vec{S} + V^T(r)S_{12}, \tag{2.2}$$

which consists of a central part V^C, a spin-orbit component V^{LS} and a tensor term V^T. Further variables of Eq. (2.2) are explained in Tab. 2.1.

Table 2.1: Notation of the variables used in Eq. (2.2).

$\vec{L}$	relative angular momentum	
$\vec{S}$	relativ spin	$\vec{S} = \vec{\sigma}_1 + \vec{\sigma}_2$
$\vec{L} \cdot \vec{S}$	spin-orbit operator	
S_{12}	tensor operator	$S_{12} = 3(\vec{\sigma}_1 \cdot \hat{r})(\vec{\sigma}_2 \cdot \hat{r}) - \vec{\sigma}_1 \cdot \vec{\sigma}_2, \quad \hat{r} = \vec{r}/\lvert\vec{r}\rvert$
$\vec{\sigma}_i$	Pauli spin matrices	
$\vec{r}$	relative distance vector	

For small momentum transfer $q \to 0$, the spin-orbit and tensor terms of the interaction are small compared to the central part. Then the effective interaction consists of components with different spin-isospin transfer properties:

$$V(\vec{r},\vec{p}) = V_0^C(r) + V_\sigma^C(r)\vec{\sigma}_1 \cdot \vec{\sigma}_2 + V_\tau^C(r)\vec{\tau}_1 \cdot \vec{\tau}_2 + V_{\sigma\tau}^C(r)\vec{\sigma}_1 \cdot \vec{\sigma}_2 \vec{\tau}_1 \cdot \vec{\tau}_2 \tag{2.3}$$

Here, spinflip transitions are caused by the spin operator $\vec{\sigma}_1 \cdot \vec{\sigma}_2$, whereas the isospin operator $\vec{\tau}_1 \cdot \vec{\tau}_2$ induces isospin-flip transitions. The energy dependence of the free nucleon-nucleon interaction in the limit $q \to 0$ is shown in Fig. 2.1. Clearly the isoscalar spin-independent term

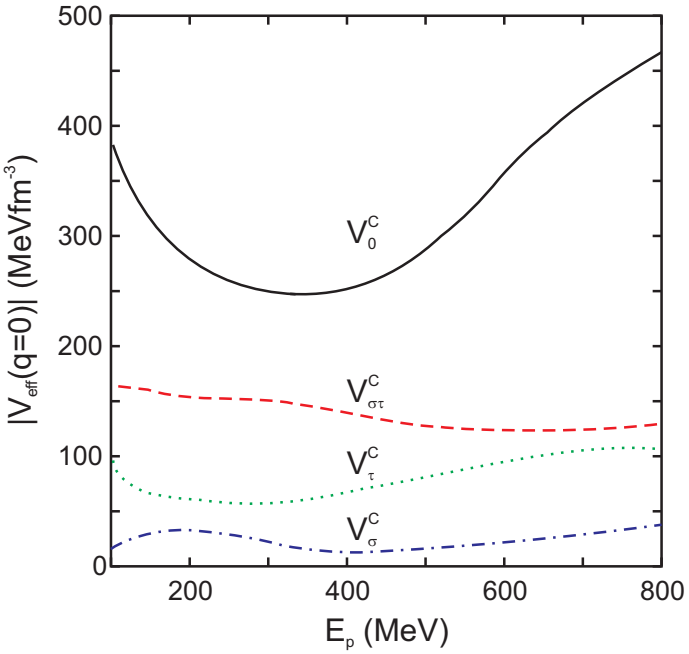

Figure 2.1: Energy dependence of the central terms of the effective nucleon-nucleon interaction from Love and Franey [17] for a vanishing momentum transfer $q \to 0$.

V_0 dominates the other terms. Spin- and/or isospin exchange between projectile and target are described by the isovector spin-dependent $V_{\sigma\tau}$, the isovector spin-independent V_τ and the

isoscalar spin-dependent V_σ parts. Since V_0 reaches a minimum in the region of 200-300 MeV, these are preferable conditions to observe isovector spinflip transitions with $\Delta L = 0$, $\Delta S = 1$ and $\Delta T = 0$ (spin M1 resonance).

2.3 Coulomb excitation

For large impact parameters $b > r_{Coulomb}$, where $r_{Coulomb} = r_p + r_t$ is the sum of the projectile and target radii, mainly Coulomb excitation is observed, since the nuclear excitation cross sections are marginal. In this case the Coulomb repulsion prevents projectile and target from approaching each other too close. Consequently the excitation cross sections are directly proportional to the transition matrix elements revealing basic nuclear structure information. Furthermore, Coulomb excitation is well understood [18], so that it is possible to extract the corresponding electromagnetic transition strengths $B(\pi\lambda)$. There are two common descriptions of this process: the excitation of a target nucleus in the electromagnetic field of a charged projectile, or vice versa, and the exchange of virtual photons between the interacting particles.

2.3.1 Classical approach

Treating the Coulomb excitation process classically, the projectile is assumed to be a point-like charge moving along a hyperbolic orbit in the repulsive field of a target nucleus with a negligible recoil. A typical trajectory of the projectile is presented in Fig. 2.2. The momentum transfer $q = |\vec{k} - \vec{k}'|$ is given by

$$q = 2mv_0 \sin\left(\frac{\theta}{2}\right), \tag{2.4}$$

with the mass m and the velocity v_0 and the scattering angle θ of the projectile. The differential elastic cross section can be calculated by the Rutherford scattering formula

$$\left(\frac{\mathrm{d}\sigma}{\mathrm{d}\Omega}\right)_{Ruth} = a^2 \frac{1}{\sin^4\left(\frac{\theta}{2}\right)}, \qquad \text{with } a = \frac{1}{4\pi\varepsilon_0}\frac{Z_1 Z_2 e^2}{4E}. \tag{2.5}$$

Evidently the beam is bend less for higher energies. Considering small momentum transfers, large cross sections due to inelastic Coulomb scattering can be expected. For relativistic projectile energies ($\beta = v/c$), Eq. (2.5) needs to be extended to the Mott formula

$$\left(\frac{\mathrm{d}\sigma}{\mathrm{d}\Omega}\right)_{Mott} = \left(\frac{\mathrm{d}\sigma}{\mathrm{d}\Omega}\right)_{Ruth}\left[1 - \beta^2 \sin^2\left(\frac{\theta}{2}\right)\right]. \tag{2.6}$$

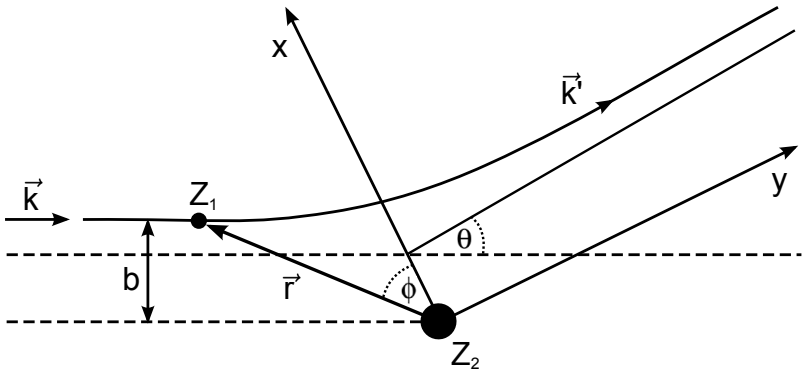

Figure 2.2: Classical projectile trajectory in Coulomb scattering. Position, momentum and deflection angle of the projectile are indicated by ϕ, $\vec{r}$, $\vec{k}$ and θ, respectively.

2.3.2 Equivalent virtual photon method

Likewise, Coulomb excitation can be regarded as the absorption of virtual photons by the target nucleus. Produced by the moving projectile, the number of virtual photons equates to the amount of real photons, which would have an equivalent net effect for one specific transition. It is linked to the Fourier transformation of the time-dependent electromagnetic field induced by the projectile. An appropriate theoretical description of this process is provided by Baur and Bertulani [19]. Here, the Coulomb excitation cross section is given by

$$\sigma_{i\to f} = \sum_{\pi\lambda} \int N_{\pi\lambda}(E_\gamma)\sigma_\gamma^{\pi\lambda}(E_\gamma)\frac{1}{E_\gamma}\mathrm{d}E_\gamma, \tag{2.7}$$

where $\sigma_\gamma^{\pi\lambda}(E_\gamma)$ is the photoabsorption cross section depending on the photon energy E_γ and $N_{\pi\lambda}(E_\gamma)$ tags the equivalent photon numbers for electric (π =E) or magnetic (π =M) transitions of multipole order λ. In a semiclassical approximation [19, 20] the virtual photon numbers can be calculated analytically for negligible energy loss of the projectile. It is based on the so-called eikonal approximation [21]. This kind of approximation originates from ray optics, where it is assumed that light travels along a straight line [22]. As long as the object is large enough compared to the wavelength of light, this assumption works quite well. However, microscopic phenomena have to be explained by Maxwell's equations with the dispersion relation $\omega = kc$. In quantum mechanics, microscopic phenomena are described by Schrödinger's equation with a dispersion relation $\omega = \hbar k^2/2m$ for small scales, too. Just as well an eikonal approximation can be adopted here for processes concerning small scattering angles and large impact parameters. This leads to

$$N_{\pi\lambda}(E_\gamma) = Z_1^2\alpha\frac{l[(2l+1)!!]^2}{(2\pi)^3(l+1)}\sum_m \left|G_{\pi\lambda m}\left(\frac{c}{v_0}\right)\right|^2 g_m(\xi), \tag{2.8}$$

with the fine structure constant $\alpha = e^2/\hbar c$ and the functions g_m and $G_{\pi\lambda m}$, which are tabulated in [20]. Similarly the double differential cross section is derived from virtual photon numbers as

$$\frac{\mathrm{d}^2\sigma}{\mathrm{d}\Omega \mathrm{d}E_\gamma} = \frac{1}{E_\gamma} \sum_{\pi\lambda} \frac{\mathrm{d}N_{\pi\lambda}}{\mathrm{d}\Omega} \sigma_\gamma^{\pi\lambda}(E_\gamma). \tag{2.9}$$

Integrating once over the energy finally yields for E1 transitions

$$\left(\frac{\mathrm{d}N_{E1}}{\mathrm{d}\Omega}\right)_{rel} = \frac{Z_1^2\alpha}{4\pi^2}\zeta^2\varepsilon^2\left(\frac{1}{\gamma\beta}\right)^2\left[K_1^2(x) + \frac{1}{\gamma^2}K_0^2(x)\right]. \tag{2.10}$$

Here, $\zeta = \omega a/v_0$ is the adiabaticity parameter with $a = Z_1 Z_2 e^2/\mu v_0^2$ referring to half of the closest distance. Additionally, μ is the reduced mass, whereas $\varepsilon = \sin^{-1}(\theta/2)$ is the eccentricity parameter and both β and γ are the relativistic parameter definitions characterizing the velocity of the projectile. The variable in $K(x)$ of the modified Bessel function of the second kind is an abbreviation for $x = (\varepsilon\zeta/\gamma)\cos(\theta/2)$. For $\gamma \approx 1$ ($\varepsilon \gg 1$) the equivalent photon number for E1 is by approximation

$$\left(\frac{\mathrm{d}N_{E1}}{\mathrm{d}\Omega}\right)_{nonrel} = \frac{Z_1^2\alpha}{4\pi^2}\varepsilon^2\left(\frac{1}{\beta}\right)^2 x^2\left[K_1^2(x) + K_0^2(x)\right]. \tag{2.11}$$

In addition, the equivalent photon numbers for other multipole orders can be deduced in the non-relativistic case:

$$\frac{\mathrm{d}N_{E2}}{\mathrm{d}\Omega} = \frac{Z_1^2\alpha}{4\pi^2}\left(\frac{1}{\beta}\right)^4\varepsilon^2 e^{-\pi\zeta/\gamma}\left[\frac{4}{\gamma^2}\left(K_1^2 + xK_0K_1 + x^2K_0^2\right) + x^2(2-\beta^2)^2K_1^2\right] \tag{2.12}$$

$$\frac{\mathrm{d}N_{M1}}{\mathrm{d}\Omega} = \frac{Z_1^2\alpha}{4\pi^2}\left(\frac{\zeta}{\gamma}\right)^2\varepsilon^4 e^{-\pi\zeta/\gamma}K_1^2 \tag{2.13}$$

As an example the virtual photon numbers are plotted in Fig. 2.3 for Coulomb excitation caused by 295 MeV protons on ^{144}Sm at $E_\gamma = 3$ MeV.

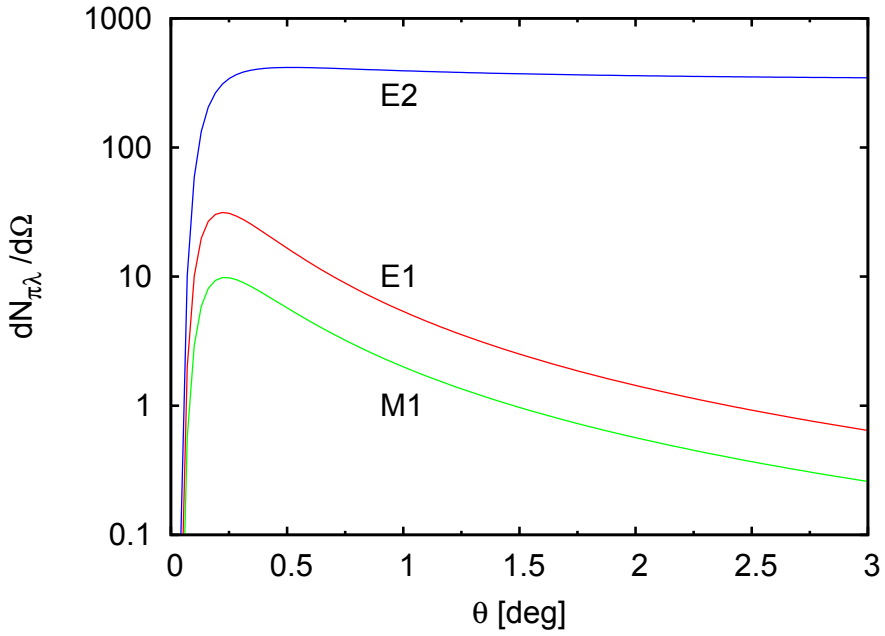

Figure 2.3: Virtual photon numbers for E1, M1 and E2 transitions caused by 295 MeV protons on ^{144}Sm at $E_\gamma = 3$ MeV calculated via Eqs. (2.11) to (2.13).

3 High resolution proton scattering experiments under 0° at RCNP

3.1 Facility

The study of the ^{144}Sm(p,p') reaction at very forward angles was performed at the Research Center for Nuclear Physics (RCNP) in Osaka, Japan. An overview of the RCNP ring cyclotron facility is shown in Fig. 3.1. Unpolarized protons from the NEOMAFIOS ECR ion source [23] were accelerated by the K = 140 MeV AVF (Azimuthally Varying Field) cyclotron up to 54 MeV. For polarized proton experiments, such as on ^{154}Sm, the ion source HIPIS [24] is used. Utilizing a six sector ring cyclotron (K400) in coupled mode, the proton beam was accelerated up to a kinetic energy of 295 MeV. Then the protons can be delivered to several experimental halls, where

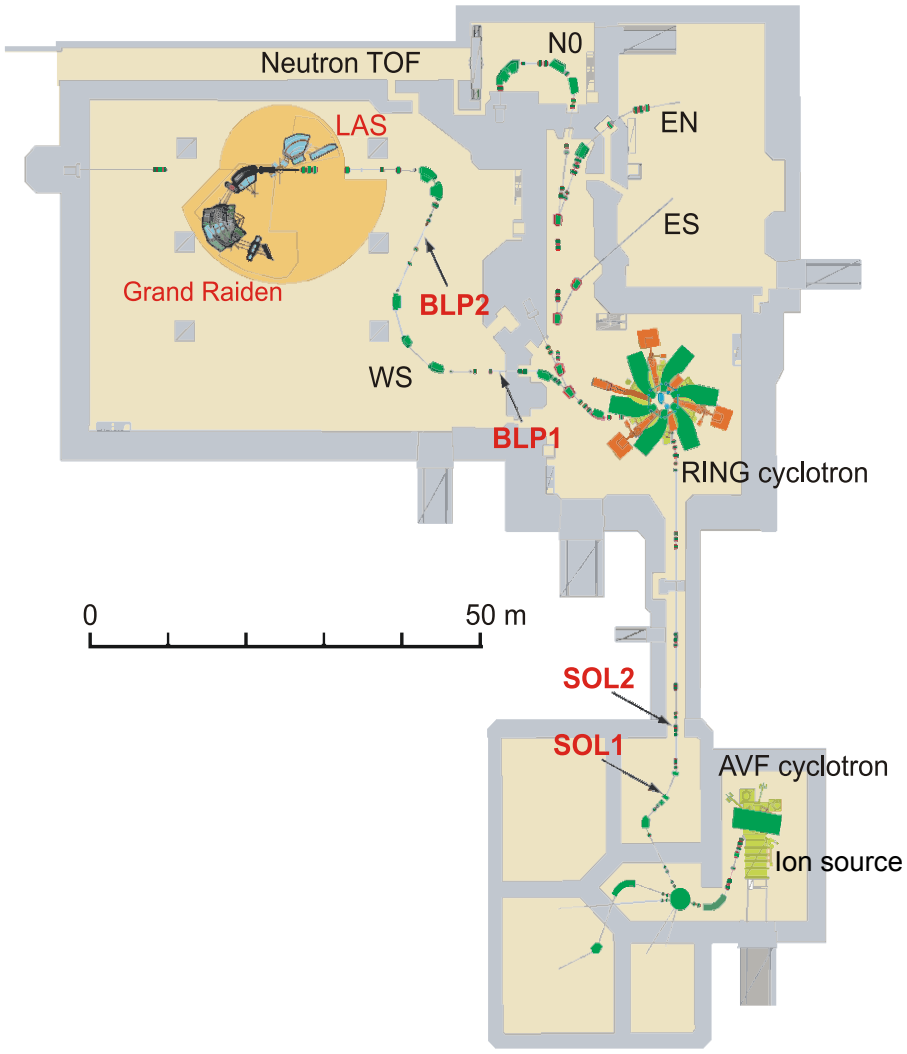

Figure 3.1: Sketch of the RCNP cyclotron facility.

a large diversity of measurements is possible. For instance unstable nuclei are studied in the East-North (EN) beam line [25], whereas the North (NO) section and a neutron-TOF setup are used for the study of spin-isospin excitations in (p,n) reactions [26]. In the present measurements the unpolarized proton beam with an energy of 295 MeV was transported to the target via the high-resolution West-South (WS) beam line. After hitting the target the inelastically scattered protons were detected with the high resolution Grand Raiden spectrometer.

3.2 Spectrometers

3.2.1 Grand Raiden

The high-resolution Grand Raiden (GR) spectrometer [27] has a Q1-SX-Q2-D1-MP-D2(+DSR) magnet configuration, where D labels dipoles, Q denotes quadrupoles, SX stands for a sextupole and MP for a multipole magnet. A dipole magnet for spin rotation (DSR), which was designed for measurements of the longitudinal polarization of scattered protons, can be optionally inserted. Figure 3.2 shows a setup of the GR spectrometer for measurements at 0°. The GR spectrometer offers a high momentum-resolution power of $p/\Delta p \approx 37000$ and a momentum acceptance of ±2.5%. Further parameters of the GR spectrometer are listed in Tab. 3.1. The detector system of the spectrometer is divided into two parts: the vertical drift chambers (VDCs) with a plastic scintillator as trigger detector and the Focal Plane Polarimeter.

3.2.2 Large Acceptance Spectrometer

The Large Acceptance Spectrometer (LAS) [28] consists of a quadrupole and a dipole. It exhibits a large solid angle and momentum acceptance of 20 msr and $\Delta p/p = 30\%$, respectively. Pairs of multiwire drift chambers and two planes of plastic trigger scintillation counters form the focal plane detector system. Further properties of the LAS are specified in Tab. 3.1 and a view is given in Fig. 3.3. It was positioned at 60° during the experiments to monitor the vertical beam position, which sensitively enters into the calibration of the scattering angles (see Ch. 4.3). The vertical angular acceptance of the LAS was reduced to ±6 mr by an entrance collimator. So the beam position resolution was improved, such that a ±0.01 mm shift of the center of the vertical beam position could be detected.

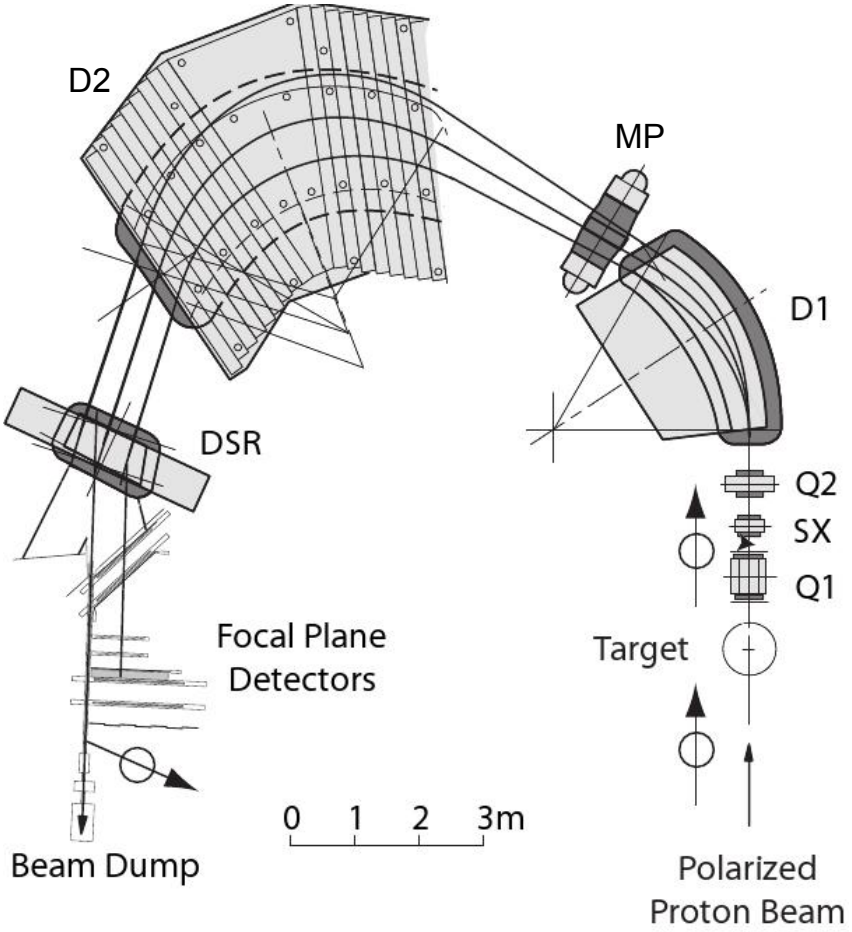

Figure 3.2: Schematic view of the GR spectrometer. D1, D2: first and second dipole magnets. Q1, Q2: first and second quadrupole magnets. SX: sextupole magnet. DSR: dipole magnet for spin rotation. MP: multipole field magnet.

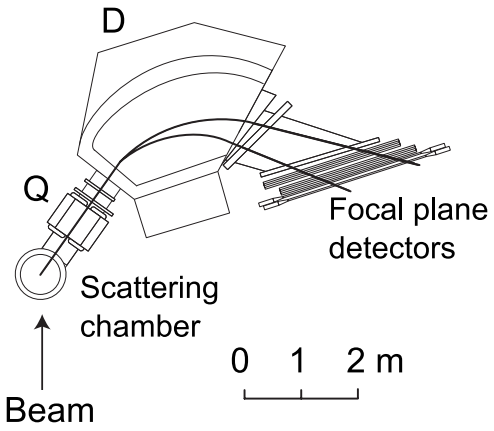

Figure 3.3: Overview of the Large Acceptance spectrometer.

Table 3.1: Specifications of GR and LAS spectrometer

	Grand Raiden (GR)	Large Acceptance spectrometer (LAS)
Configuration	QSQDMDD	QD
Mean orbit radius	3 m	1.5 m
Total deflecting angle	180°	70°
Tilting angle of focal line	45°	57°
Maximum magnetic rigidity	5.4 Tm	3.2 Tm
Vertical magnification	5.98	-7.3
Horizontal magnification	-0.417	-0.4
Momentum range	5 %	30 %
Momentum resolution	37 075	4 980
Acceptance of horizontal angle	±20 mr	±60 mr
Acceptance of vertical angle	±70 mr	±100 mr

3.3 Detector Systems

The detector system of the GR spectrometer is built up of two principal constituents: the Focal Plane Detector System (FPDS) [29] and the Focal Plane Polarimeter (FPP) [30]. A schematic view of the setup is shown in Fig. 3.4.

The FPDS comprises two multi-wire chambers of the vertical type, the so-called vertical drift chambers (VDCs) and a plastic trigger scintillation counter with a thickness of about 3 mm, which determined the energy loss of scattered protons for the particle identification. It was used to reconstruct the necessary parameters of the reaction, e.g. the scattering angles and the excitation energy of the particles. Overall, four parameters x_{fp}, θ_{fp}, y_{fp}, ϕ_{fp} were measured by two sets of VDCs. x_{fp} and θ_{fp} are intersection point and angle of the particle in the focal plane, respectively, whereas y_{fp} and ϕ_{fp} denote those in the non-dispersive plane of the system.

When scattered particles pass through the chamber, the working gas is ionized and electron-ion pairs are produced. By measuring the drift times of the electrons in the electric field of the chamber, the particle rays in the plane perpendicular to the wires can be reconstructed. Every VDC consists of two sets of wire planes (X and U), which are sandwiched between three cathode planes. Since the X planes are stretched perpendicular to the dispersion direction of the GR spectrometer, information regarding x_{fp} and θ_{fp} are detected by theses planes. Tilted to an angle of 48.19° relative to the X plane wires, the U planes are responsible for the determination of the intersection point and intersection angle in the non-dispersive plane. A high voltage of -5.6 keV was applied to the cathode planes of the VDCs, the potential wires were set to -0.3 keV and the sense wires remained at ground level. The drift chambers were filled with a gas mixture of argon (71%), iso-buthane (29%) and iso-propyl-alcohol.

The FPP, which forms the second part of the detector system, can be utilized to measure the polarization of the scattered protons. If the polarized protons pass through the carbon analyzer, the nuclear spin-orbit interaction leads to an azimuthal asymmetry in the scattering from carbon nuclei. The particle trajectories as well as the scattering angles in the carbon block are determined by four multi-wire proportional chambers (MWPCs) in front of and behind the carbon slab (see Fig. 3.4). As scattering processes for polarized protons are well known, it is possible to draw conclusions from the angular distribution of the protons behind the carbon block to the polarization of the protons [31]. More detailed information can be found in [11].

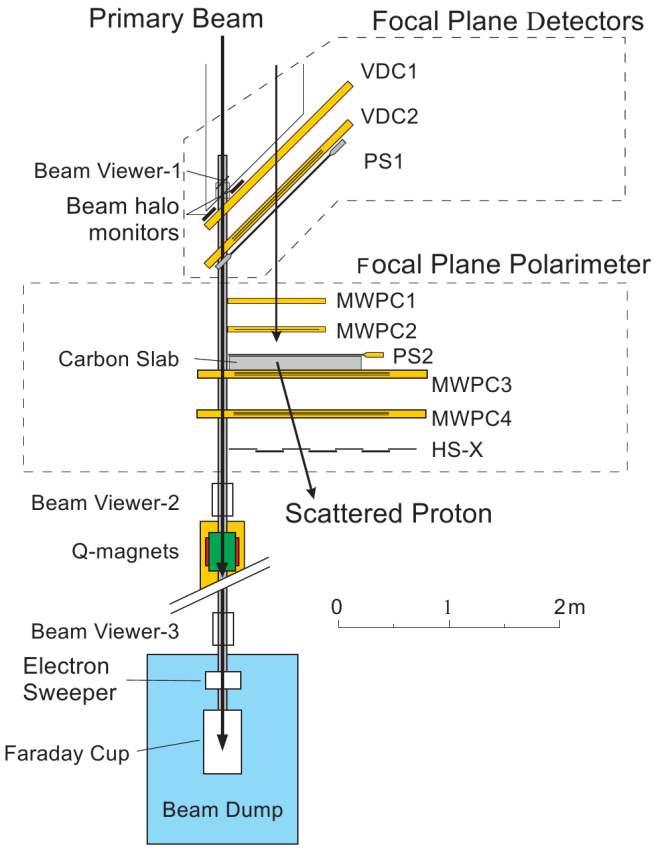

Figure 3.4: Layout of the GR detector system. The VDCs are used for position and angle determination of the scattered particles at the focal plane. Polarization measurements of scattered particles can be performed in the focal plane polarimeter.

3.4 Experimental conditions

In May 2011 (p, p') scattering experiments on ^{144}Sm and ^{154}Sm were performed at the RCNP facility in Osaka. In particular also $(\vec{p}, \vec{p}')$ scattering was measured on ^{154}Sm, in order to distinguish spinflip and non-spinflip transitions via polarization transfer observable analysis. The measurements were accomplished under scattering angles of 0° and 3° during a time of 14 days. All in all a measurement time of 8 hours under 0° and 4 hours under 3° was collected for ^{144}Sm.

As a stable halo-free beam is fundamental to gain clean spectra, beam tuning plays an important role in the measurement procedure [32]. Initially an unpolarized beam with an energy spread smaller than 50 keV is tuned employing the achromatic transport mode at finite angles. Thereafter, a halo-free beam is set up for inelastic scattering measurements under 0°. For polarization experiments polarized protons are tuned with respect to low energy spread, too. In the end lateral and angular dispersion matching [33] is applied leading to an energy resolution of about 25 keV (FWHM).

For the calibration of the ion optics of the GR spectrometer, elastic proton scattering was measured with a sieve slit target under 16°. In addition, elastic scattering runs for future target thickness determination were performed under angles of 9°, 10°, 12° and 13.5°. All experimental conditions are summed up in Tabs. 3.2 and 3.3.

Table 3.2: Summary of the common experimental conditions

Proton beam energy	295	MeV
Energy resolution (achromatic, ^{197}Au and ^{27}Al)	40	keV
Energy resolution (dispersive with faint beam)	18	keV
Energy resolution (dispersive, ^{208}Pb)	25	keV

Table 3.3: Summary of the experimental conditions in each measurement

Measurement	0°	forward angle	elastic
Transport mode	dispersive	dispersive	achromatic
GR angle	0°	3°	9°, 10°, 12°, 13.5°, 16°
Beam intensity	6 nA	6 nA	6 nA

3.5 Targets

Metallic self-supporting foils of ^{154,144}Sm with a thickness of 4.0 mg/cm^2 and an isotopical enrichment of 98.69% and 85.91%, respectively, were used as targets. Further constituent parts of the ^{144}Sm foil are listed in Tab. 3.4. The beam tuning and resolution checks in the

Table 3.4: Abundance of further isotopes in the ^{144}Sm foil. The uncertainties are less than 3% of the listed values.

Sm isotope	abundance
147	3.88%
148	2.18%
149	2.19%
150	1.02%
152	2.80%
154	2.02%

achromatic mode were performed with a ^{197}Au foil with a thickness of 1.68 mg/cm^2. For background and halo faint beam measurements a blank target frame was utilized. Furthermore, ^{26}Mg (2.5 mg/cm^2) was used for the energy calibration using several well-known peaks with high statistics [34]. A ^{58}Ni (100.1 mg/cm^2) target was utilized for the calibration measurement of the complicated ion-optical system in the GR spectrometer. For a comparison to former experiments, spectra of ^{120}Sn (6.5 mg/cm^2) and ^{208}Pb (5.2 mg/cm^2) were measured.
In order to reduce background, all targets were mounted on an aluminum frame instead of an usual stainless steel frame. The aluminum frames were placed on a moveable target ladder, which is shown in Fig. 3.5, at the center of the scattering chamber.

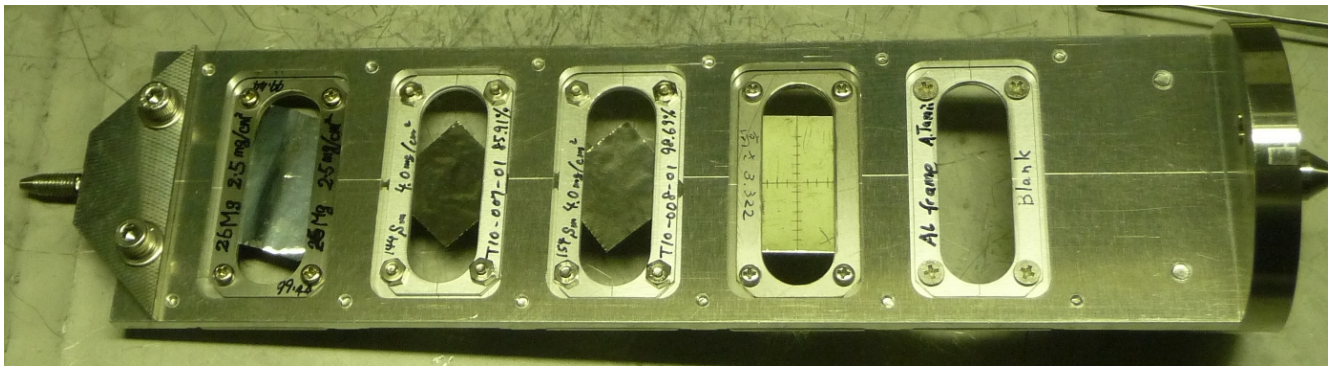

Figure 3.5: Placement of the target foils on the target ladder.

3.6 Principle of the under-focus mode

In order to maintain a good scattering angular resolution an under-focus mode was used during the measurements. Under very forward angles including 0° the precise determination of the scattering angle in both the horizontal (dispersive) and vertical (non-dispersive) direction plays an important role. The total scattering angle at the focal plane is given by $\theta_{fp} = \sqrt{(\theta_t + \theta_{GR})^2 + \phi_t^2}$, where θ_t is the horizontal, ϕ_t is the vertical scattering angle at the target and θ_{GR} is the angle, to which the GR spectrometer was set. With normal field settings, vertical and horizontal scattering angles of the scattered protons are focused at the focal plane. However, due to the small magnification factor of the GR spectrometer, which is 5.98 (see Tab. 3.1), the vertical scattering angle resolution becomes worse than 20 mrad. To prevent this loss of acceptance, a vertical off-focus mode (over-focus or under-focus) was applied by changing the magnetic field of the Q1 magnet. The resulting optical path of the particles is illustrated in Fig. 3.6. Since the dependence of the vertical ion-optical parameters on the horizontal scattering angles is smaller, a mild under-focus mode leads to better accuracy of the measured scattering angles. Therefore the field of the Q1 quadrupole was decreased by 5%.

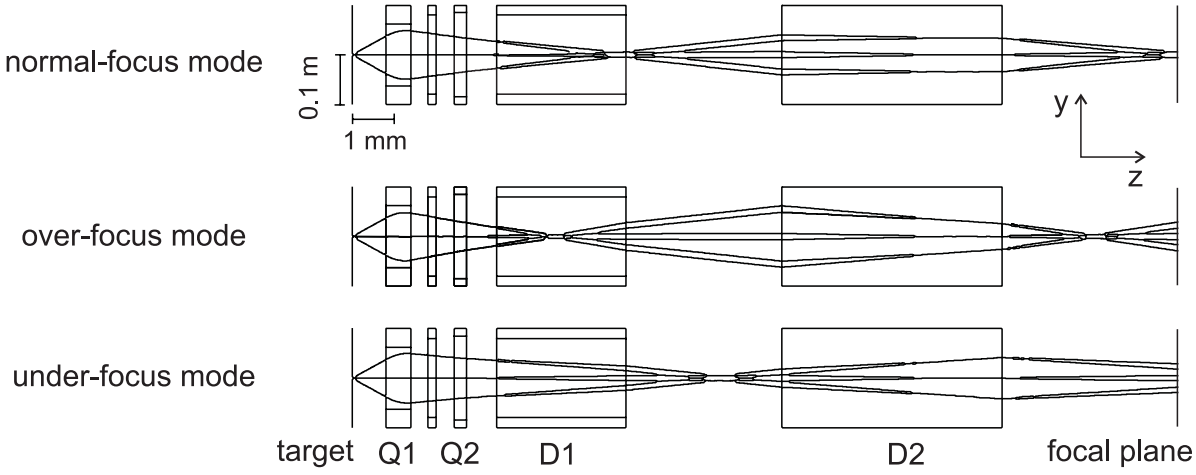

Figure 3.6: The vertical beam trajectories in the $y - z$ plane for scattered particles with $\phi_t = 0, \pm 46$ mrad and $y_t = \pm 1$ mm in three different focus modes of GR optics.

3.7 Sieve slit measurements

Since scattered protons pass through the complicated ion-optical system of the GR spectrometer, the image of an object is deformed at the focal plane. Consequently, so-called sieve slit measurements were performed to reconstruct scattering angles at the target position from the scattering information. A brass plate ("sieve slit") with a thickness of 5 mm and 25 holes was inserted into the beam line 638 mm downstream of the target at the entrance of the GR spectrometer. The alignment of the holes was 5 (horizontal) × 5 (vertical) and is shown in Fig. 3.7. Due to a better adjustment, the center hole had a diameter of 3 mm, which equals 4.7 mrad in the scattering angle. The other holes had a diameter of 2 mm (3.1 mrad). The horizontal distance between the center of the holes was 4.5 mm (7 mrad). Vertical distances are 12 mm (19 mrad) respectively.

The GR spectrometer was moved to a laboratory scattering angle θ_{lab}=16 °, as the differential cross section of elastic proton scattering on ^{58}Ni shows a flat angular distribution at this angle. Protons, which passed a slit or were scattered through a slit, could be detected at the focal plane. In order to account for the dependence of the scattering angles on the horizontal position at the focal plane, the magnetic field strength values were changed by +1.2%, +1.8%, 2.6%, 3.4% and +4.2% relative to the standard setting. These values correspond to excitation energies of 6, 10, 14, 18 and 22 MeV, respectively. Hence, the whole excitation energy range of the experiments could be covered. To determine the influence of the beam position on the target, measurements were performed with the beam spot in the center and ±1 mm shifts in vertical direction.

All in all fifteen sets of data were taken to find the ion-optical parameters of the GR spectrometer. The calibration of the scattering angles by the sieve slit analysis is discussed in Sec. 4.3.

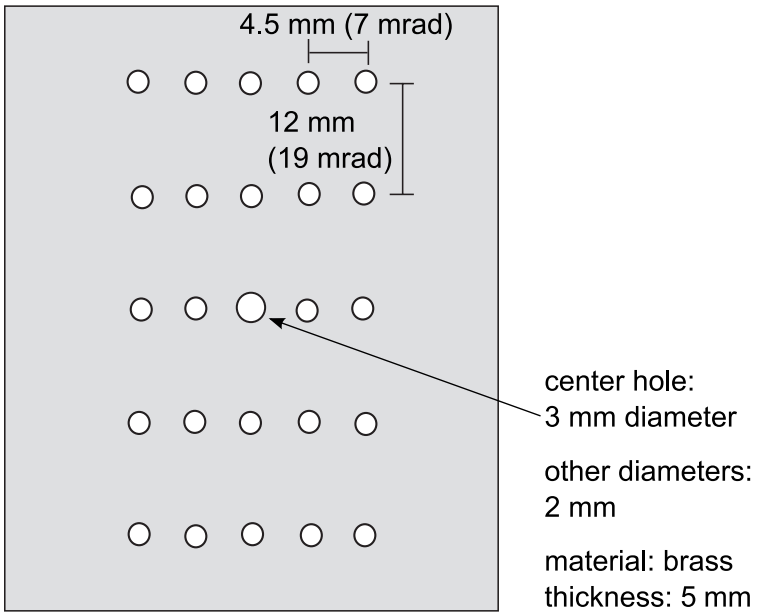

Figure 3.7: Layout of the sieve slit plate.

4 Data analysis

For the data analysis the program code ANALYZER [11] was used, which was developed at the RCNP to analyze data obtained at the GR and the LAS spectrometers. It is mainly written in C and utilizes the HBOOK and PAW++ packages from the CERN libraries [35]. The analysis and calibration procedure is divided into the following steps

- Conversion from drift times to drift length,
- Determination of the efficiency of VDCs,
- Calibration of scattering angles,
- Correction of high-order aberrations of the GR spectrometer,
- Excitation energy calibration,
- Background subtraction.

Each step will be discussed in the subsequent chapters.

4.1 Drift time to drift distance conversion

In the vertical drift chambers (VDCs) the position of the scattered protons is measured in order to reconstruct their trajectory, which is necessary for the analysis of the excitation energy and the incident angles.

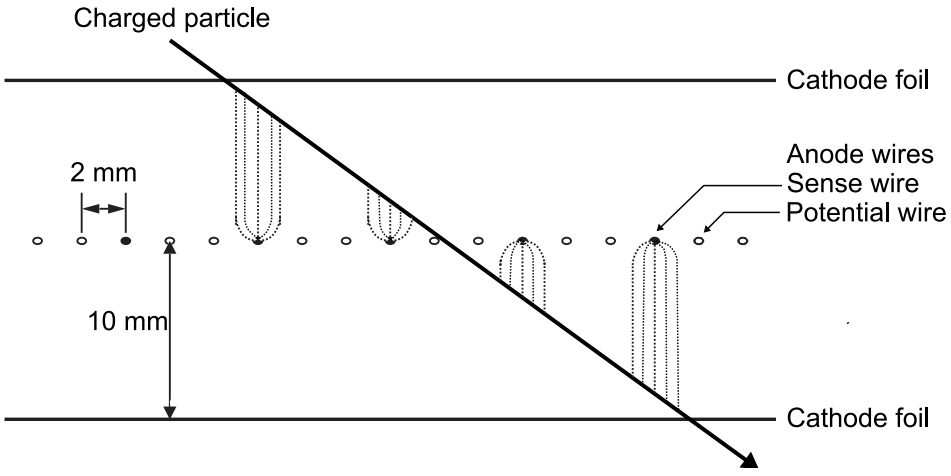

Figure 4.1: Schematic view of a plane of a vertical drift chamber. The track of a charged particle track between the two cathode planes is shown. The drift ways to the sense wires are denoted as dotted lines.

When charged particles pass through the detector, they collide with molecules of the working gas and ionize them. Electron-ion pairs thus created drift in the applied electric field with an approximately constant velocity of about 5 cm/μs towards the anode plane. Using the signal of multiple wires the drift distance can be deduced from the drift time. As the electric field increases close to sense wires avalanche multiplication happens, however the potential wires stay at ground potential.

The reconstruction is illustrated schematically in Fig. 4.1. The time difference between the wire signal and the delayed signal of the plastic scintillator is determined by time-to-digital converters (TDCs). These TDC values need to be converted into drift distances. Therefore a white spectrum with homogeneously distributed events was measured, which is shown in Fig. 4.2 on the top of the left hand side. After the conversion, the drift length histogram has a flat distribution (Fig 4.2, bottom of the l.h.s.). The histogram on the r.h.s. shows the proportionality between TDC channels and the drift length. Due to the field inhomogeneity close to sense wires, deviations from linearity occur for large TDC channel numbers.

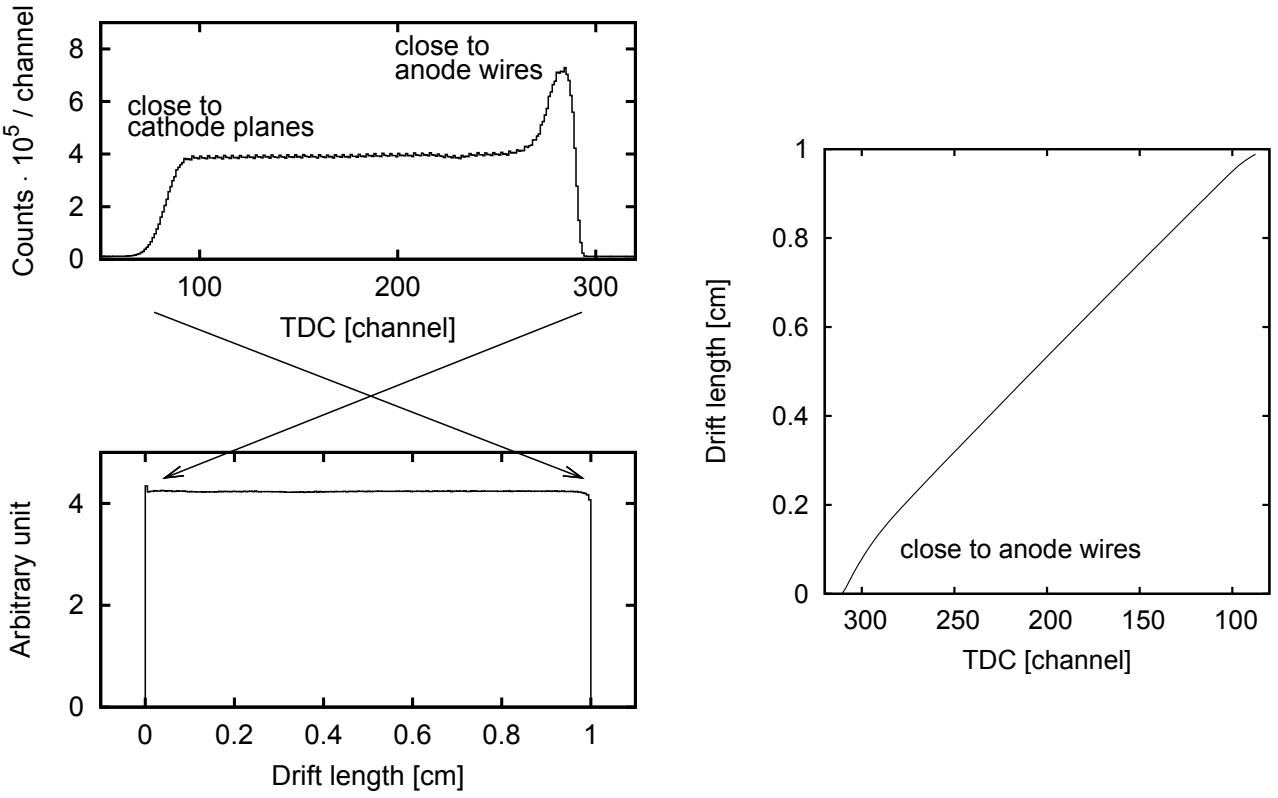

Figure 4.2: Conversion of drift time to drift length for the VDCs. Exemplary the histograms for the GR spectrometer X2 VDC are shown. After the conversion the drift length obeys a flat distribution.

As the VDCs are set up under an angle of 45°, the particles induce signals at more than two wires, when they cross the chambers. Therefore neighboring events are grouped as clusters and clusters with single hits are discarded, i.e. clusters, in which only one wire provides a signal.

Also the wire with the shortest signal is neglected, since the non-uniformly electric field near the sense wires leads to uncertainties in the conversion from drift time to drift length as shown in Fig. 4.2. The intersection point of the trajectory at the wire plane is calculated by a least-square fit from the drift lengths of wire signals. Taking the information of all wire planes it is possible to determine the trajectory and the scattering angle of the particles.

4.2 Efficiency of the VDCs

The detection efficiency of the VDCs was calculated for each wire plane as the ratio between the number of events, for which intersection positions were successfully determined for four wire planes, and the number of events for the other three planes. For instance, the efficiency of the X1 plane is

$$\epsilon_{X1} = \frac{N_{X1,X2,U1,U2}}{N_{X1,X2,U1,U2} + N_{\overline{X1},X2,U1,U2}}, \tag{4.1}$$

where $N_{X1,X2,U1,U2}$ is the number of events, in which the cluster positions can be determined for all planes. $N_{\overline{X1},X2,U1,U2}$ stands for the number of events, in which the cluster positions can be determined for all planes but the X1 plane. The efficiencies of the other wire planes were obtained in the same way. The individual efficiencies of all four wire planes were about 93-97%. The product of the four efficiencies gives the total efficiency:

$$\epsilon_{total} = \epsilon_{X1}\,\epsilon_{X2}\,\epsilon_{U1}\,\epsilon_{U2} \tag{4.2}$$

The average total of the whole experiment was 88%.

4.3 Sieve slit analysis

With the data of the sieve slit measurements described in Ch. 3.7 the scattering angles at the target θ_t and ϕ_t can be reconstructed from the positions and scattering angles at the focal plane. The horizontal scattering angle θ_t at the target position mainly depends on the horizontal incident angle θ_{fp} at the focal plane, whereas the vertical scattering angle ϕ_t is essentially determined by the vertical position y_{fp} at the focal plane. Hence the vertical LAS position y_{LAS} (Fig. 4.3(b)) has to be considered for the correction of the vertical scattering angle, too. Additionally, both of the scattering angles depend on the horizontal position x_{fp} at the focal plane. The sieve slit analysis allows to determine these dependencies.

A spectrum of elastic scattering events is presented in Fig. 4.3(a). The gray area denotes the gate on x_{fp}, which is used for the sieveslit analysis, and the bump around $x_{fp} = -10$ mm arises from elastic scattered events passing through the brass plate with an energy loss of about

10 MeV. Having applied the gate for the elastic events, the remaining events can be inspected in the $\theta_{fp} - y_{fp}$ plane, which is illustrated in Fig. 4.3(c). In order to examine the centers of all spots, the two-dimensional plot of $\theta_{fp} - y_{fp}$ was sliced into five rectangles horizontally and vertically. Examples are shown by gray shapes in Fig. 4.3(c). Each vertical slice was projected onto the θ_{fp} axis, whereas each horizontal slice was projected onto the y_{fp} axis. The projections onto the axes are also shown in Fig. 4.3(c). Via Gaussian fits both the θ_{fp}- and the y_{fp}-position of the spots were extracted, assuming a round shape of the hole images. Scattering at the opening of the sieve slits was neglected. Afterwards the correlation between θ_{fp} and ϕ_{fp} was

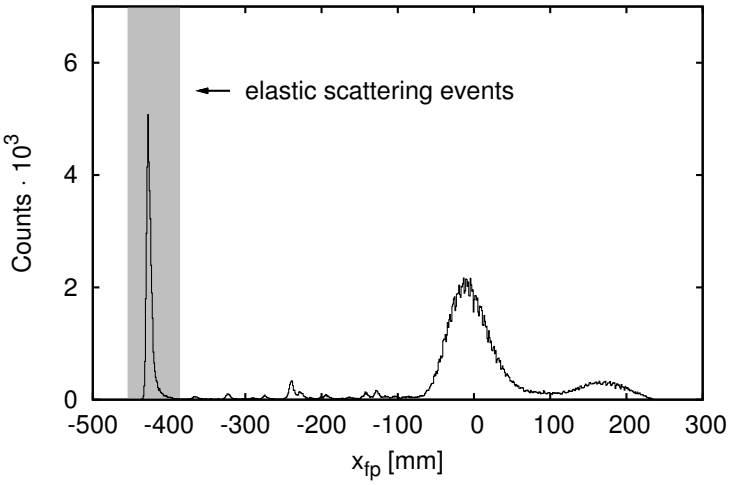

(a) Gate for elastic scattering events.

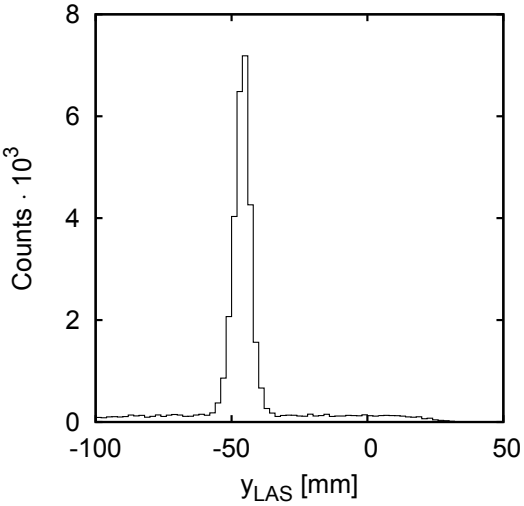

(b) Vertical position of the beam monitored in the LAS spectrometer.

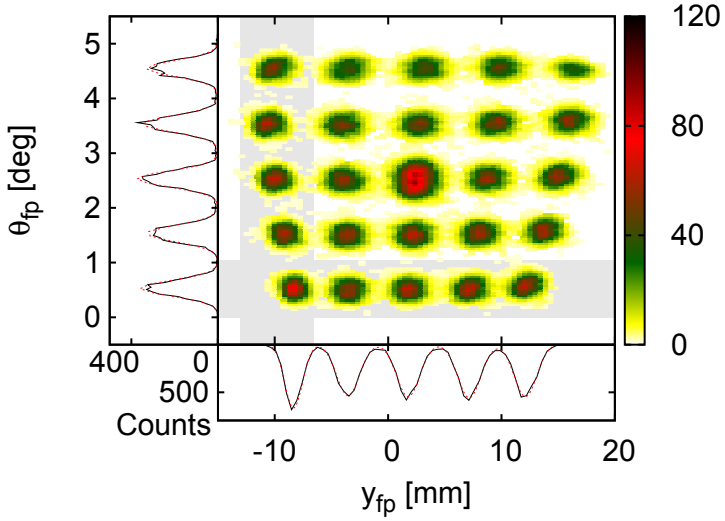

(c) Horizontal scattering angle at the focal plane θ_{fp} against y_{fp}.

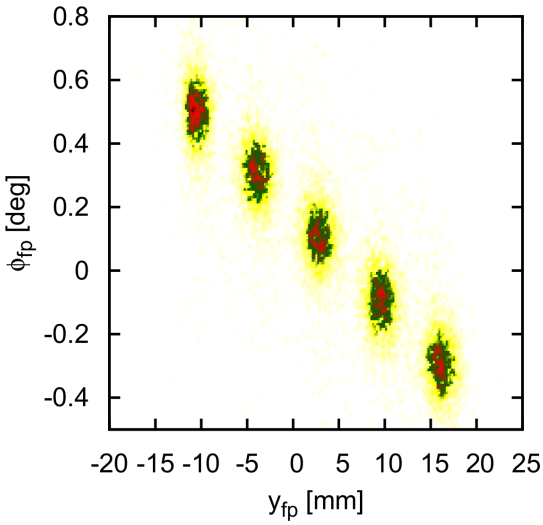

(d) Vertical scattering angle at the focal plane ϕ_{fp} against y_{fp}.

Figure 4.3: Extraction of y_{LAS}, θ_{fp}, y_{fp} and ϕ_{fp} from the sieve slit analysis.

explored by setting specific gates on θ_{fp}. Thus the $y_{fp} - \phi_{fp}$ plot in Fig. 4.3(d) was evaluated by projecting the events onto the ϕ_{fp} axis and fitting Gaussians again.

Finally, the vertical and horizontal scattering angles were calculated with a multi-dimensional least square fit routine utilizing the GNU scientific library (GSL) [36]. Former studies [37] showed that mixed terms for the determination of the scattering angles are several orders of magnitudes lower than the first-order terms. Mixed terms are summands, which either consist of polynomials with a degree higher than one or depend on at least two different variables of x_{fp}, θ_{fp}, y_{fp}, ϕ_{fp} and y_{LAS}. Due to their marginal impact on the fitting results they were omitted.

$$\theta_t(x_{fp}, \theta_{fp}) = \sum_{i=0}^{1}\sum_{j=0}^{1} a_{ij} \cdot x_{fp}^i \, \theta_{fp}^j \tag{4.3}$$

$$\phi_t(x_{fp}, \theta_{fp}, y_{fp}, \phi_{fp}, y_{LAS}) = \sum_{i=0}^{1}\sum_{j=0}^{1}\sum_{k=0}^{1}\sum_{l=0}^{1} b_{ijkl} \cdot x_{fp}^i \theta_{fp}^j y_{fp}^k \phi_{fp}^l + \sum_{m=0}^{1} c_m \cdot x_{fp}^m y_{LAS} \tag{4.4}$$

The resulting coefficients for the present experiment are listed in Tab. 4.1. Figure 4.3 shows the reconstruction of the sieve slit holes using Eqs. (4.3) and (4.4).

Table 4.1: Table of coefficients for Eqs. (4.3) and (4.4) for the reconstruction of scattering angles. The numbers of i, j, k and l represent the exponent of x_{fp}, θ_{fp}, y_{fp} and ϕ_{fp}, respectively. All angles are given in radian and all distances in mm. The omitted coefficients are set to zero.

$i\,j$	coefficients a_{ij}
00	$3.380 \cdot 10^{-2}$
01	$-3.958 \cdot 10^{-1}$
10	$3.837 \cdot 10^{-5}$

$i\,j\,k\,l$	coefficients b_{ijkl}
0000	$-4.619 \cdot 10^{-2}$
0001	2.681
0010	$-1.529 \cdot 10^{-3}$
1000	$2.590 \cdot 10^{-5}$

m	coefficients c_m
0	$-1.012 \cdot 10^{-3} \cdot y_{LAS}$
1	$4.130 \cdot 10^{-7} \cdot y_{LAS}$

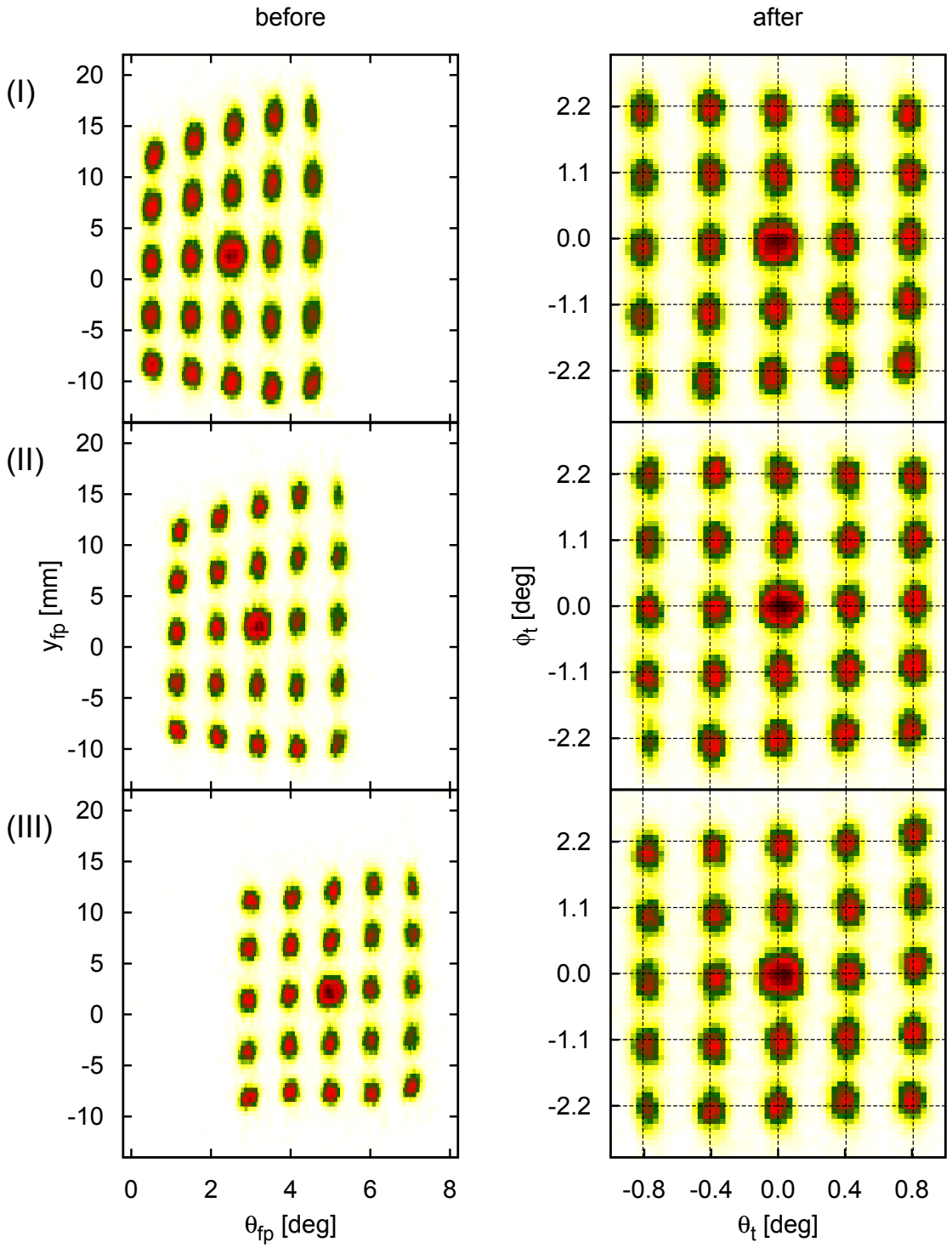

Figure 4.4: Two-dimensional $y - \theta$ histograms before and after corrections according to Eqs. (4.3) and (4.4) and using the parameters of Tab. 4.1. The images (I), (II) and (III) correspond to kinetic energies of 6, 10 and 18 MeV, respectively. The crossings of dotted lines in the right part represent the actual holes in the sieve slit. Due to the calibration the center of the events should coincide with the crossing points.

The offset coefficients (a_{00} and b_{0000}) were measured at the beginning of the beam time via optical position determination methods. As this procedure contains large uncertainties and since the sieveslit was removed and reserted again for the sieveslit measurements three weeks later, the initial values of these coefficients were not consistent any more. Thus, the final values for a_{00} and b_{0000} were reconstructed by software corrections. The fitting results for each hole of the sieve slit yield a horizontal scattering angle resolution of 0.14° (FWHM) and a vertical angular resolution of about 0.5° (FWHM). The systematic uncertainties in the determination of the scattering angles were established via the deviation of the corrected spot centers from the true spot centers. Their values were less than 0.1° for the horizontal direction and less than 0.25° for the vertical direction.

4.4 Kinematic corrections and energy calibration

The recoil effects in the reaction kinematics for the nuclei ^{144}Sm and ^{154}Sm were calculated with the program KINMAT [38] and afterwards fitted with gnuplot [39]. In the case of elastic scattering and a proton energy of 295 MeV it is

$$E(\theta) = -7.28 \cdot 10^{-4}\,\theta^2\ \text{MeV/deg}^2 + 295\ \text{MeV} \quad \text{for} \quad ^{144}\text{Sm}, \tag{4.5}$$

$$E(\theta) = -6.80 \cdot 10^{-4}\,\theta^2\ \text{MeV/deg}^2 + 295\ \text{MeV} \quad \text{for} \quad ^{154}\text{Sm}. \tag{4.6}$$

In Fig. 4.5 the energy of the scattered protons is plotted considering the recoil of ^{144}Sm.

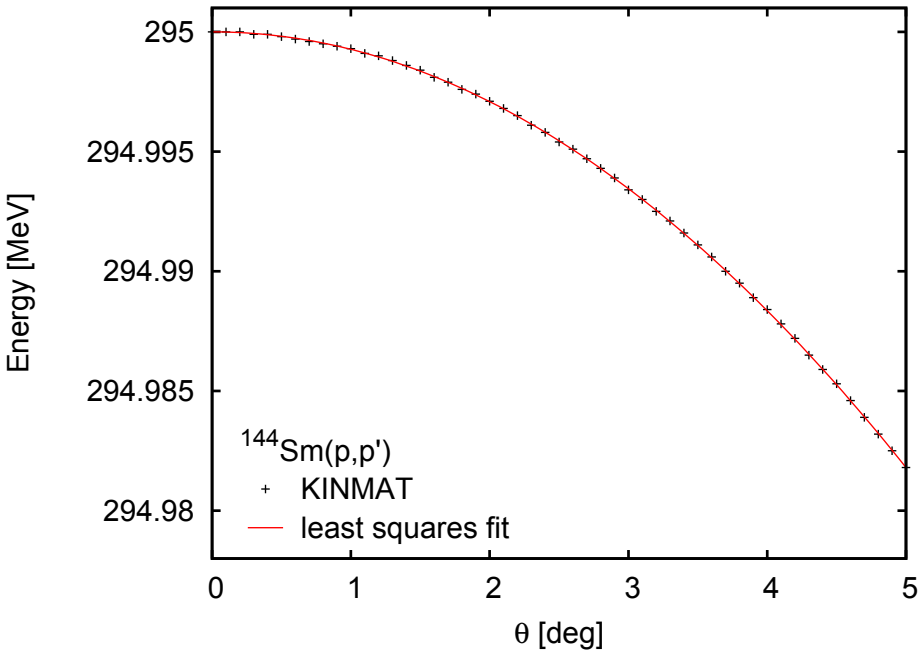

Figure 4.5: Kinematical dependence of the scattered protons on recoil effects of ^{144}Sm. The red line indicates the fit of Eq. (4.5) and the crosses are the calculations with the code KINMAT.

However, there still remains an interconnection between θ_{fp} and x_{fp} due to the ion-optic properties of the GR spectrometer. Therefore, several spectra of ^{26}Mg were analyzed, which show well-known discrete peaks in the region from 9 MeV to 13 MeV [34]. Examples of the curved line shapes for these transitions are shown in the upper part of Fig. 4.6. In order to straighten the lines and improve the position (and thus momentum) information, a polynomial function

$$x_c = x_{fp} + \sum_{i=0}^{1}\sum_{j=1}^{4} d_{ij} \cdot x_{fp}^{i}\, \theta_{fp}^{j} \tag{4.7}$$

was fitted to each of them. Applying the corrections of Eq. (4.7) leads to the θ_{fp}-x_c-plot shown in the lower part of Fig. 4.6. Clearly the resolution in x_c, and accordingly in the reconstructed energy, is improved. The resulting coefficients of the above fit procedure for the present data are listed in Tab. 4.2.

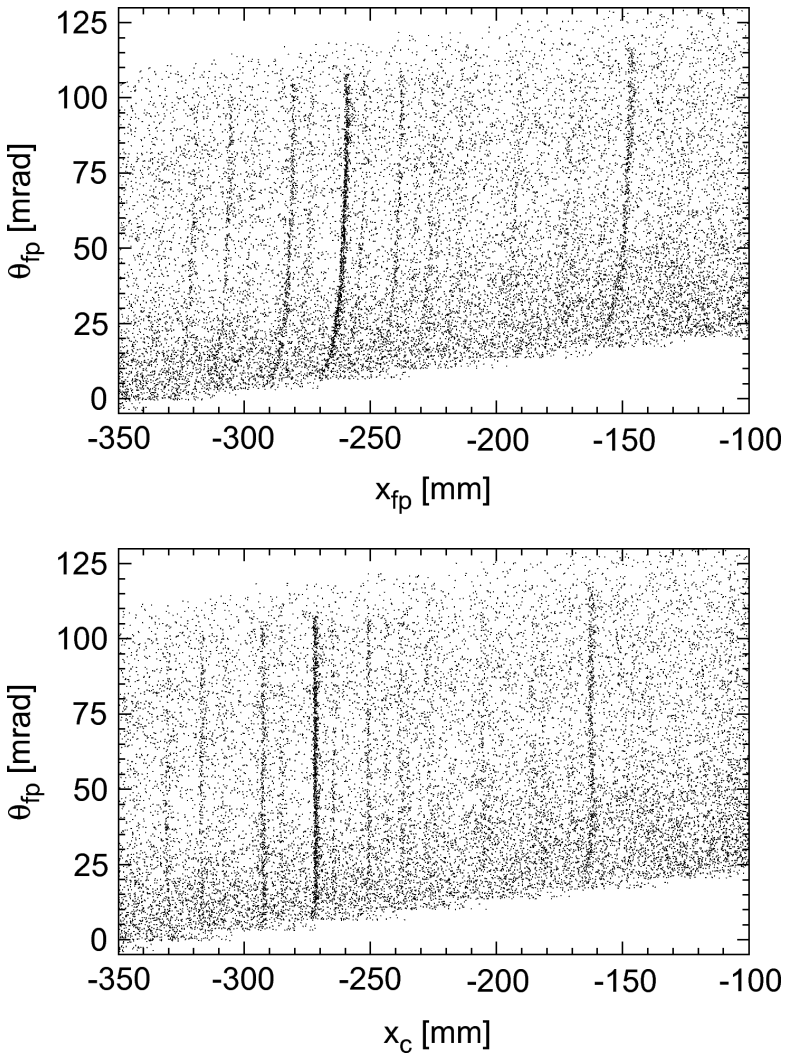

Figure 4.6: Two-dimensional histograms of the $x_{fp} - \theta_{fp}$ plane for the ^{26}Mg(p,p') reaction before the software corrections (top) and after the straightening of the lines (bottom), with a fit to Eq. (4.7).

Table 4.2: Table of coefficients for Eq. (4.7) for the correction of x_{fp}. The numbers of i and j represent the exponent of x_{fp} and θ_{fp}, respectively. All angles are given in radian and all distances in mm.

$i\,j$	coefficients d_{ij}
01	$-2.856 \cdot 10^{2}$
02	$-1.784 \cdot 10^{3}$
03	$4.607 \cdot 10^{4}$
04	$-1.960 \cdot 10^{5}$
11	$8.515 \cdot 10^{-1}$
12	$-4.269 \cdot 10^{1}$
13	$5.073 \cdot 10^{2}$
14	$-1.938 \cdot 10^{3}$

After the corrections described in the previous chapters, the energy calibration was performed next. Six well-known peaks in the ^{26}Mg excitation energy spectra were used. Their horizontal positions x_c obtained by Gaussian fits and the corresponding excitation energies taken from the Evaluated Nuclear Structure Data File (ENSDF) [40] are listed in Tab. 4.3.

Table 4.3: Transitions used for the energy calibration. All corrected horizontal positions are given in mm and all corresponding excitation energies taken from [40] in keV.

x_c	Δx_c	E_x	ΔE_x
-319.743	0.044	9238.7	0.5
-305.908	0.035	9560	3
-280.900	0.021	10148	2
-273.700	0.020	10319	2
-259.583	0.012	10645	2
-252.487	0.037	10805.9	0.4

For the conversion of position to excitation energy a linear function was assumed, which leads to the equation

$$E_x(x_c) = 23.93 \cdot 10^{-3}\ \text{MeV/mm} \cdot x_c + 17.14\ \text{MeV}, \tag{4.8}$$

where x_c ranges from -600 mm to $+600$ mm. Likewise, polynomial functions of second and third order were fitted to the data of Tab. 4.3, but the resulting uncertainties were large compared to those of the linear fit of Eq. (4.8). A calibrated energy excitation spectrum of ^{26}Mg is shown in Fig. 4.7. Since the beam energy slightly differs for each run, this calibration had to

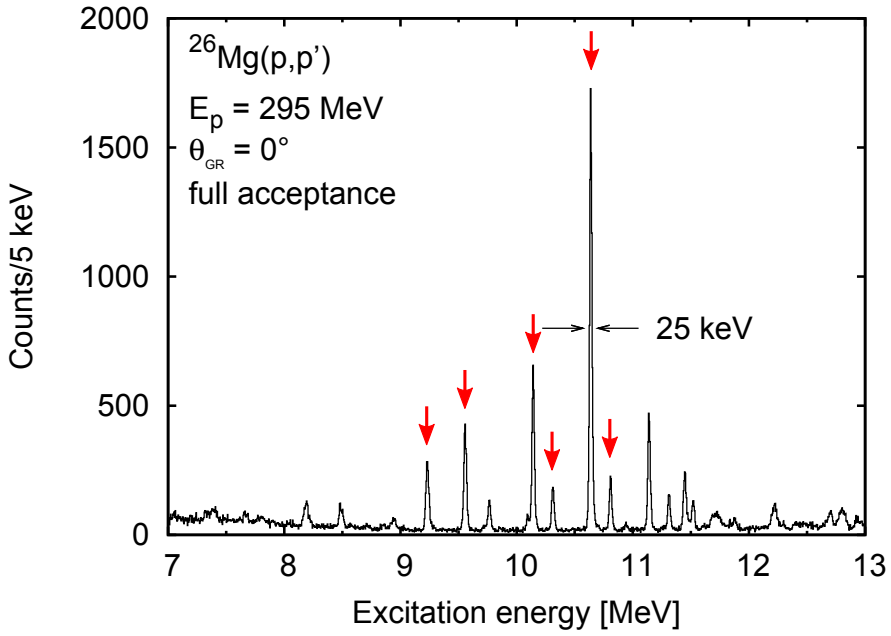

Figure 4.7: Excitation energy calibration with the ^{26}Mg(p,p') reaction. The peaks, which were chosen for a least square fit (see Tab. 4.3), are indicated by red arrows. Here, the energy resolution was 25 keV (FWHM).

be performed for all runs separately. Therefore, energy shifts were defined, in order to achieve that the strongest peak (at 10.645 MeV $\pm$ 2 keV) of a single ^{26}Mg spectrum coincides with the same one of all calibrated ^{26}Mg energy excitation spectra. This method comprises a systematical uncertainty of less than 5 keV.

4.5 Background subtraction

Even under the best experimental conditions and with successful beam tuning, instrumental background remains. As it mainly originates from multiple scattering of protons within the target foil, background events are uniformly distributed and consequently they ideally obey a flat distribution in the non-dispersive focal plane. Then the true events are focused at $y_{fp} = 0$ and can be distinguished from background events. Thus a transformation of the coordinate y_{fp} in the non-dispersive direction was performed with a least-square fit method, in order to calculate the dependence of the corrected position y_c on x_{fp}, y_{fp}, θ_{fp}, ϕ_{fp} and y_{LAS}. This yields the relation

$$y_c = y_{fp} + \sum_{i=0}^{1}\sum_{j=0}^{1}\sum_{k=0}^{1} f_{ijk} \cdot x_{fp}^{i}\, \theta_{fp}^{j}\, \phi_{fp}^{k} + f_l \cdot y_{LAS}, \tag{4.9}$$

where the coefficients f_{ijk} and f_l are fitting parameters, whose values for the present data are listed in Tab. 4.4. For this transformation, data obtained during the sieveslit measurements were used.

Table 4.4: Table of coefficients for Eq. (4.9) for the correction of y_{fp}. The numbers of i, j and k represent the exponent of x_{fp}, θ_{fp} and ϕ_{fp}, respectively. All angles are given in radian and all distances in mm. The omitted coefficients are set to zero.

$i\,j\,k$	coefficients f_{ijk}
000	$2.645 \cdot 10^{1}$
001	$1.092 \cdot 10^{3}$
010	$-1.952 \cdot 10^{1}$
011	$2.088 \cdot 10^{3}$
100	$6.969 \cdot 10^{-3}$
101	$-7.908 \cdot 10^{-1}$
111	-5.919

l	coefficient f_l
0	$6.197 \cdot 10^{-1} \cdot y_{LAS}$

The correction of y_{fp} is shown in the right panel of Fig 4.8 in comparison to the uncorrected results (lhs.). In the background subtraction method referred to as the "conventional method", the background is removed by setting a narrow gate on the region around $y_c = 0$. Afterwards the background events in this narrow central gate are estimated by assuming a flat distribution and taking the average of two background gates applied to the pure background regions next to the central gate (see e.g. [12, 13]). However this method is very sensitive on the choice of these background gates and it does not work satisfactorily, when scattering angle cuts for the solid angle of the spectrometer are applied [34]. Also, some correlation between y_c and ϕ_t remains.

That is why a new background subtraction method was developed called the "extended method" [10]. It eliminates the dependence of y_c on the scattering angle ϕ_t by respecting the relations of Eq. (4.4) and introduces the corrected scattering angle ϕ_c, independent of y_c. Here, the essential assumption is that the background events are homogeneously distributed in the vertical acceptance of the spectrometer, i.e. in the $y_c - \phi_c$ plane. Therefore another correction, which is analogue to the one for y_{fp}, is performed with respect to ϕ_{fp}.

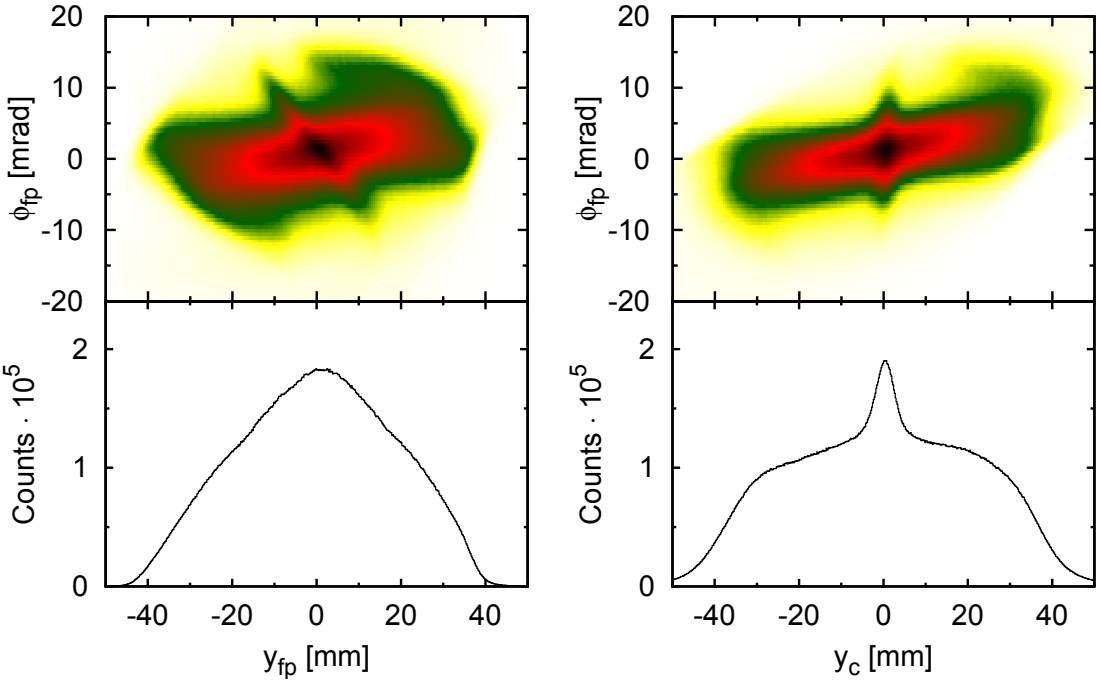

Figure 4.8: Correlation between the vertical scattering angle ϕ_{fp} and the vertical position y_{fp} before (lhs.) and after (rhs.) the transformation via Eq. (4.9).

This correction is given by the equation

$$\phi_c = \phi_{fp} + \sum_{i=0}^{1} e_i \cdot y_{fp}^i, \tag{4.10}$$

where the coefficients e_i denote fitting parameters. The corrected $y_c - \phi_c$ plane is illustrated in Fig. 4.9(a). Still, the true events are distributed in an upright-shaped region around $y_c = 0$ as indicated by the 2D gate. In the following step, two sets of artificially shifted data were created by adding (subtracting) a constant to (from) y_{fp}. Thus y_c was shifted, too, without affecting ϕ_c.

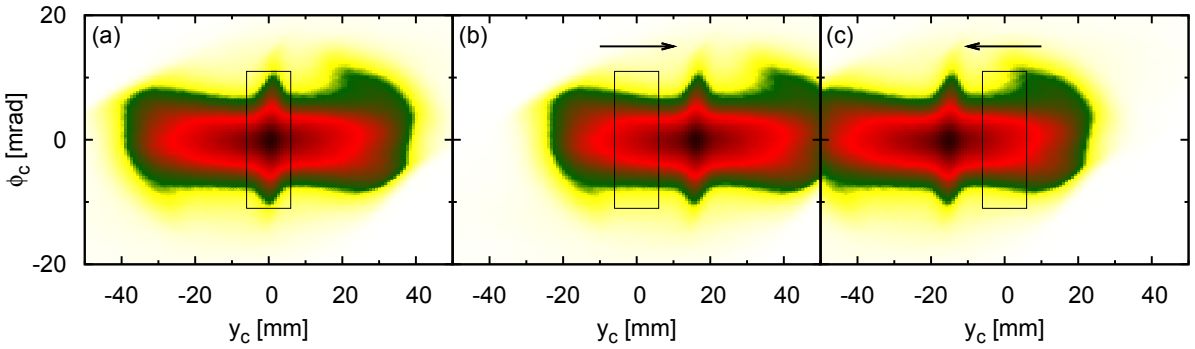

Figure 4.9: Method of background subtraction with the corrections of Eq. (4.10). Only events in the black boxes were analyzed. The arrows show the direction of the applied shifts.

The choice of this constant depends on the excitation energy, however the obtained background should be independent of the displacement direction. Examples for these displaced sets of data are presented in Figs. 4.9(b) and 4.9(c). The shifted histograms were analyzed in exactly the same way as the unshifted data. Especially the identical software gates were applied. Taking the average of the two displaced data sets, a background spectrum was obtained, conserving the same complicated corrections among all gates [41]. In Fig. 4.10, the resulting excitation energy and background spectra are shown. The bump around 7.5 MeV in both spectra originates from a target in the beam line polarimeter, which had been inserted for previous polarization transfer measurements. Subtracting the background spectrum leads to the spectrum in the left part of Fig. 4.11, extracted within the full acceptance of the GR spectrometer, i.e. in a scattering angle region of 0° – 0.7° horizontally and 0° – 2° vertically. The right side of Fig. 4.11 shows the background-subtracted spectrum for the 3° measurements, where an acceptance of 0° – 1° horizontally and 0° – 3° vertically was included. Both spectra contain the characteristical bump in the giant resonance area arising from the Coulomb excitation of the GDR.

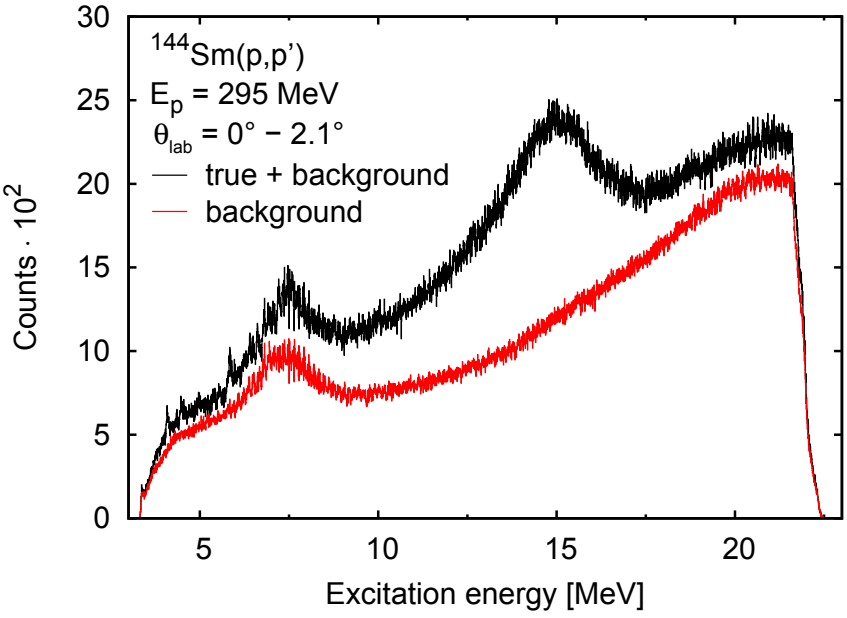

Figure 4.10: Excitation energy spectrum (black) and background spectrum (red) of the ^{144}Sm(p,p') reaction at $E_p = 295$ MeV and $\theta_{GR} = 0°$ obtained with the "extended method" (see text).

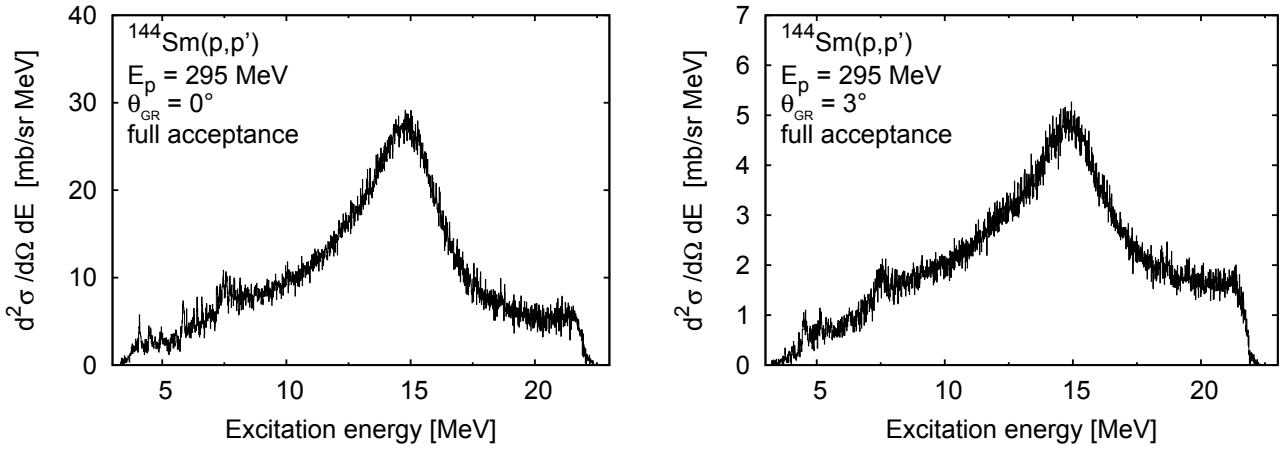

Figure 4.11: Background subtracted spectra for the $^{144}\mathrm{Sm}(p,p')$ reaction at 0° (lhs.) and 3° (rhs.).

4.6 Cross section extraction

Using the experimental parameters listed in Tab. 4.5 double differential cross sections were calculated by the equation

$$\frac{\mathrm{d}^2\sigma}{\mathrm{d}\Omega \mathrm{d}E} = N_{Counts}\frac{1}{\Omega_{Lab}}\frac{1}{L\epsilon}\frac{e}{Q}\frac{A}{N_A t\eta}J. \tag{4.11}$$

Results are shown in Fig. 4.11. Due to quasi-free nucleon scattering [42] the count rate - and therefore the double differential cross section - increases in the region from 18.5 MeV to 22.5 MeV for slightly higher scattering angles. After all corrections the final energy resolution of the spectra was about 25-30 keV.

Table 4.5: Variables entering into Eq. (4.11), and their values.

N_{Counts}	yield for the specific energy bin		[Counts/MeV]
Ω_{Lab}	solid angle in the laboratory frame		[sr]
L	DAQ live time ratio		
ϵ	detector efficiency		
e	elementary charge	$1.602 \cdot 10^{-19}$	[C]
Q	collected charge		[C]
A	target atomic weight	144	[g/mol]
N_A	Avogadro number	$6.023 \cdot 10^{23}$	[1/mol]
t	target thickness	4.0	[g/cm^2]
η	target enrichment	85.91%	
J	Jacoby transformation from lab to center of mass system		

The statistical and systematical uncertainties were determined by the equations

$$\Delta \left.\frac{\mathrm{d}^2\sigma}{\mathrm{d}\Omega \mathrm{d}E}\right|_{stat} = \frac{1}{\sqrt{N_{Counts}}} \frac{\mathrm{d}^2\sigma}{\mathrm{d}\Omega \mathrm{d}E}, \tag{4.12}$$

$$\Delta \left.\frac{\mathrm{d}^2\sigma}{\mathrm{d}\Omega \mathrm{d}E}\right|_{sys} = \sqrt{\left(\frac{\Delta\epsilon}{\epsilon}\right)^2 + \left(\frac{\Delta L}{L}\right)^2 + \left(\frac{\Delta t}{t}\right)^2 + \left(\frac{\Delta\Omega}{\Omega}\right)^2 + \left(\frac{\Delta Q}{Q}\right)^2} \frac{\mathrm{d}^2\sigma}{\mathrm{d}\Omega \mathrm{d}E}. \tag{4.13}$$

The leading contributions to the systematic inaccuracies originate from the determination of the solid angle (5-8%), collected charge (3-5%) and target inhomogeneity (≈5%). Accordingly the systematic uncertainties are not exceeding 10%. As the average count rates for the PDR region are roughly 400 counts per energy bin, the systematical uncertainties are less than 5%.

Since in the region around the centroid of the GDR mainly E1 transitions are expected, theoretical calculations of the differential Coulomb excitation cross section can be compared to the experimental data. Hence the double differential cross sections in the GDR interval from 14.35 MeV to 15.35 MeV was integrated over the excitation energy E_x for several scattering angle cuts. The results are shown in Fig. 4.12, where the red curve indicates the theoretical predictions calculated by the program DWEIKO (Distorted Wave EIKOnal Approximation) [43]. Clearly, this model describes the experimental values very well. Various rectangular scattering

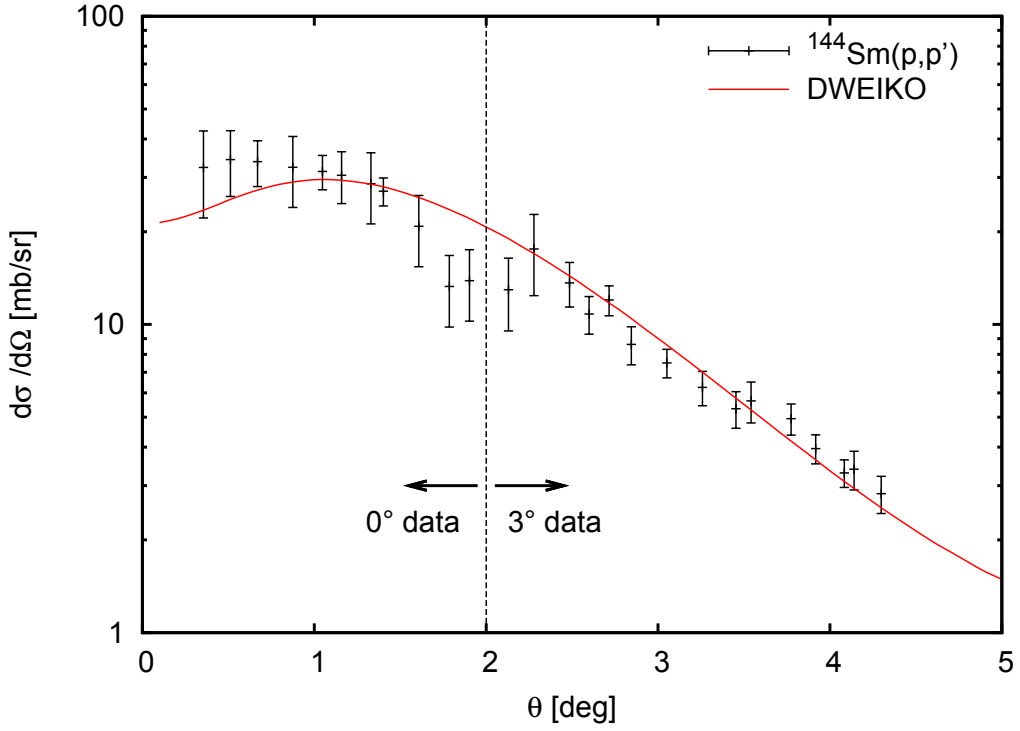

Figure 4.12: Angular distributions of the differential cross section for the GDR region around 14.85 MeV. The red curve was obtained by DWEIKO calculations [43].

angle cuts were applied to determine differential cross sections for scattering angles between 0° and 4.5°. However, the shape of the true events is not exactly rectangular shaped in exterior regions of the whole acceptance. Thus the signal to background noise ratio becomes smaller in these angle cuts and the acceptance is overestimated. That is why the differential cross sections around a scattering angle of 2° are smaller than expected for both the 0° and the 3° measurements.

4.7 Comparison with (γ, γ') data

The photoresponse of the semi-magic nucleus ^{144}Sm has been measured below 10 MeV via nuclear resonance fluorescence at the S-DALINAC in 2001 [8]. As the spectrum of the (γ, γ') experiment has an energy resolution of a few keV, it was convolved with a Gaussian, which had a width of $\Delta E = 30$ keV (FWHM) corresponding to the energy spread of the (p, p') data. The comparison of the spectra is illustrated in Fig. 4.13, where the peaks were scaled arbitrarily to coincide within an energy range from 6 MeV to 7 MeV roughly. Up to an energy of about

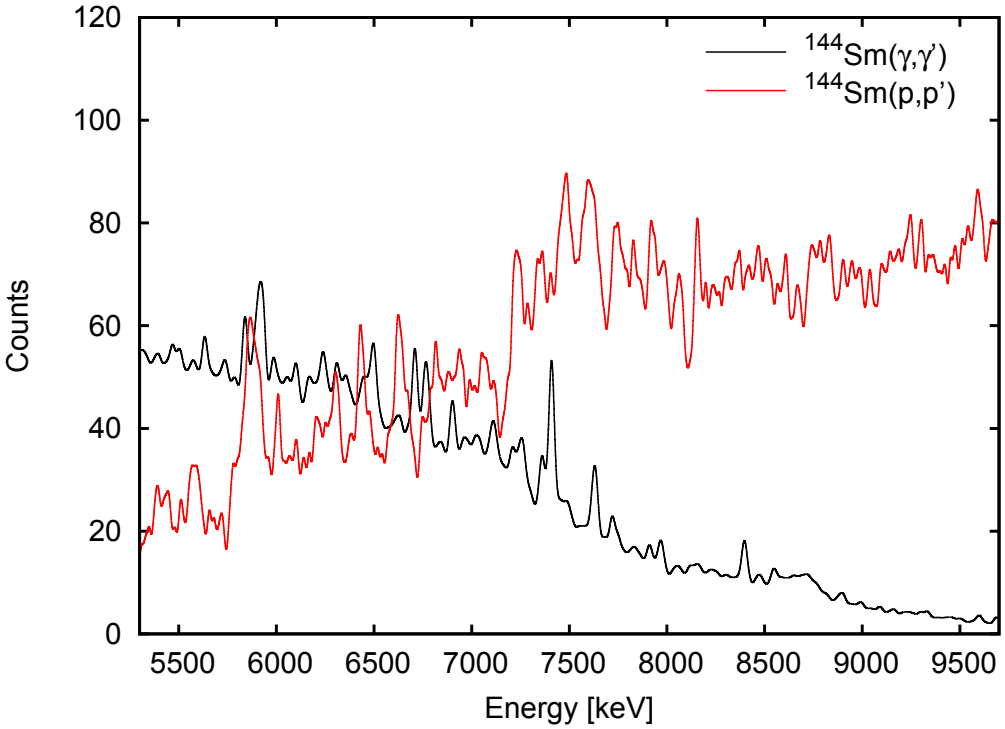

Figure 4.13: Comparison with the excitation energy spectrum of the ^{144}Sm(γ, γ') reaction [8]. The (p, p') data are indicated by red lines, whereas the (γ, γ') spectrum is plotted with black lines.

7.5 MeV similar structures are visible, however some of the peaks in the (p, p') spectrum seem to overlap so that they appear as one broad peak. Additionally, contributions to the cross sections due to M1 excitations are expected to be larger in the proton scattering. Visibly the count rates

of the (γ, γ') data strongly decrease for energies higher than 7 MeV due to decreasing efficiency and photon flux close to the endpoint energy of 9.9 MeV.

5 Summary and outlook

In conclusion, this thesis reports on the analysis of a measurement of the ^{144}Sm(p,p') reaction. Using a proton beam with an energy of $E = 295$ MeV, excitation energy spectra up to 20 MeV were obtained at very forward angles including 0°. Due to the beam tuning and the software corrections a high energy resolution of $\Delta E = 25 - 30$ keV (FWHM) was achieved. Based on these excellent conditions, a model independent background subtraction was performed, which kept all the complex correlations among the applied software gates. Therefore differential cross sections could be calculated and were determined to agree well with the theoretical predictions of the program DWEIKO. Finally the results were compared to a ^{144}Sm(γ,γ') spectrum qualitatively.

As a next step, in order to assign the spin and parity of excited states in the PDR region, a multipole decomposition must be done utilizing theoretical RPA (random phase approximation) amplitudes and single-particle wave functions calculated within the quasiparticle phonon model (QPM). Then the total E1 strength can be extracted and compared to ^{144}Sm(γ,γ') experiments. Additionally a wavelet analysis will be applied to the GDR for the identification of characteristic scales [44] and level densities of 1^- states can be extracted [45]. In combination with the analysis of the ^{154}Sm$(\vec{p},\vec{p}')$ data the impact of deformation on the PDR and the spin-M1 resonance can be clarified.

A New target thickness determination method

So far, the thickness has been determined by the ratio of the weight and the surface area of the target. Although this method involves uncertainties less than 5%, a new technique for the target thickness determination was developed to check the results with an independent procedure. In future, the target thickness shall be determined via elastic scattering measurements at several angles. Accordingly this new method was applied to ^{120}Sn and ^{208}Pb scattering data of the year 2008. The target thickness was calculated from the equation

$$\left(\frac{\mathrm{d}\sigma}{\mathrm{d}\Omega}\right)_{elastic} = N \frac{1}{\Omega_{Lab}} \frac{1}{L\epsilon} \frac{e}{Q} \frac{A}{N_A t \eta} J, \tag{A.1}$$

where N is the elastic count rate in the whole acceptance of the GR spectrometer and all the other variables refer to the ones, which are listed in Tab. 4.5. Furthermore the uncertainty relations of Eqs. (4.12) and (4.13) were employed, in order to check the consistency with the present method. The elastic differential cross sections were taken from [46] as well as [47] and are plotted in Fig. A.1, respectively. Since the differential cross sections for ^{120}Sn (in the right

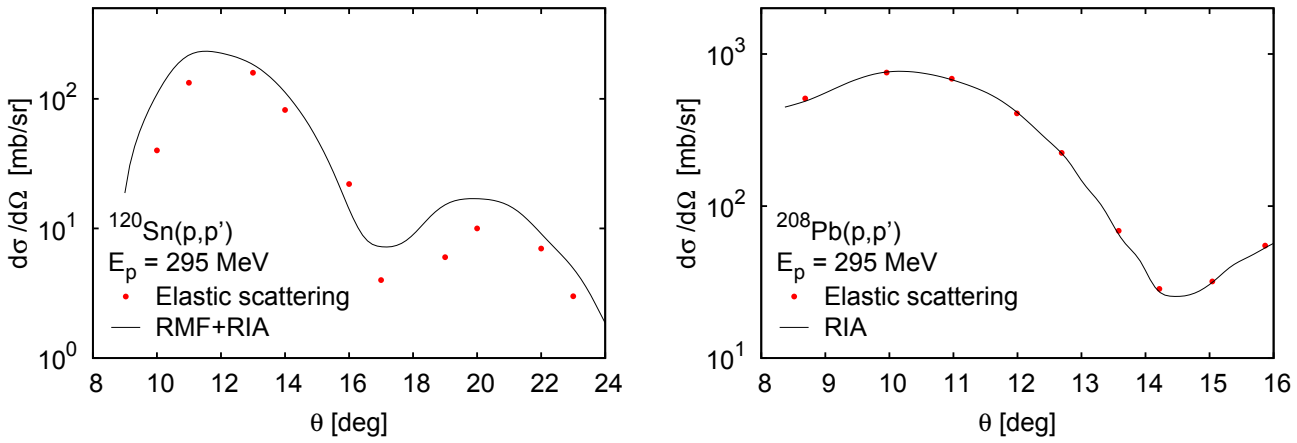

Figure A.1: Angular distribution of the elastic differential cross section of ^{120}Sn [46] (left panel) and ^{208}Pb [47] (right panel) at $E = 295$ MeV. The solid lines denote relativistic mean field (RMF) and relativistic impulse approximation (RIA) predictions [46, 47] and references therein.

part of Fig. A.1) deviate strongly from each other, calculations for experimental and theoretical values were performed separately. A reading error of about 10% was assumed for the elastic differential cross sections.

The resulting target thickness values were $t = (6.1 \pm 0.6)$ mg/cm^2 (using the experimental differential cross sections) and $t = (7.5 \pm 0.8)$ mg/cm^2 (utilizing the theoretical differential

cross sections) for ^{120}Sn, whereas for ^{208}Pb a target thickness of $t = (4.8 \pm 0.5)$ mg/cm^2 was determined.

Obviously, the results are in good agreement with the previously determined target thicknesses of 6.5 mg/cm^2 for ^{120}Sn and 5.2 mg/cm^2 for ^{208}Pb within the measurement inaccuracies. However the uncertainties of the values obtained by the new method are still very high, which is mainly on account of the elastic differential cross sections. Huge improvements concerning this new technique will be achieved, when high-precision differential cross sections are provided.

References

[1] M. N. Harakeh and A. van der Woude, *Giant Resonances in Nuclei: Fundamental High-Frequency Modes of Nuclear Excitations* Clarendon Press (2001).

[2] W. Andrejtscheff, C. Kohstall, P. von Brentano, C. Fransen, U. Kneissl, N. Pietralla and H. H. Pitz, *Phys. Lett. B* 506 (2001) 239.

[3] G. A. Bartholomew, E. D. Earle, A. J. Ferguson, J. W. Knowles and M. A. Lone, *Adv. Nucl. Phys.* 7 (1972) 229.

[4] E. Litvinova, H. P. Loens, K. Langanke, G. Martìnez-Pinedo, T. Rauscher, P. Ring, F.-K. Thielemann and V. Tselyaev, *Nucl. Phys. A* 823 (2009) 159.

[5] T. Hartmann, M. Babilon, S. Kamerdzhiev, E. Litvinova, D. Savran, S. Volz and A. Zilges, *Phys. Rev. Lett.* 93 (2004) 192501.

[6] B. Özel, *Study of the ^{112,120}Sn (γ,γ') reaction and systematics of the pygmy dipole resonance at the Z=50 shell closure*, Ph.D. thesis, Çukurova University, Adana, Turkey (2008).

[7] R. Schwengner, G. Rusev, N. Tsoneva, N. Benouaret, R. Beyer, M. Erhard, E. Grosse, A. R. Junghans, J. Klug, K. Kosev, H. Lenske, C. Nair, K. D. Schilling and A. Wagner, *Phys. Rev. C* 78 (2008) 064312.

[8] S. Volz, N. Tsoneva, M. Babilon, M. Elvers, J. Hasper, R.-D. Herzberg and H. Lenske, *Nucl. Phys. A* 779 (2006) 1.

[9] N. Ryezayeva, T. Hartmann, Y. Kalmykov, H. Lenske, P. von Neumann-Cosel, V. Yu. Ponomarev, A. Richter, A. Shevchenko, S. Volz, and J. Wambach, *Phys. Rev. Lett.* 89 (2002) 272502.

[10] A. Tamii, Y. Fujita, H. Matsubara, T. Adachi, J. Carter, M. Dozono, H. Fujita, K. Fujita, H. Hashimoto, K. Hatanaka, T. Itahashi, M. Itoh, T. Kawabata, K. Nakanishi, S. Ninomiya, A. B. Perez-Cerdan, L. Popescu, B. Rubio, T. Saito, H. Sakaguchi, Y. Sakemi, Y. Sasamoto, Y. Shimbara, Y. Shimizu, F. D. Smit, Y. Tameshige, M. Yosoi and J. Zenhiro, *Nucl. Instr. Meth. A* 605 (2009) 3.

[11] A. Tamii, *Polarization transfer observables from proton inelastic scattering from ^{12}C at zero degrees*, Ph.D. thesis, Kyoto University, Japan (1999).

[12] I. Poltoratska, *Complete dipole response in ^{208}Pb from high-resolution polarized proton scattering at 0°*, Ph.D. thesis, TU Darmstadt, Germany (2011).

[13] A. M. Heilmann, *Complete electric dipole response in ^{120}Sn: A test of the resonance character of the pygmy dipole resonance*, Master thesis, TU Darmstadt, Germany (2009).

[14] J. Simonis, Bachelor thesis, TU Darmstadt, in preparation.

[15] A. Krugmann, Ph.D. thesis, TU Darmstadt, in preparation.

[16] C. Nair, A. R. Junghans, M. Erhard, D. Bemmerer, R. Beyer, E. Grosse, K. Kosev, M. Marta, G. Rusev, K. D. Schilling, R. Schwengner and A. Wagner, *Phys. Rev. C* 81 (2010) 055806.

[17] W. G. Love and M. A. Franey, *Phys. Rev. C* 24 (1981) 1073.

[18] C. A. Bertulani and G. Baur, *Nucl. Phys. A* 442 (1985) 739.

[19] C. A. Bertulani and G. Baur, *Phys. Reports* 299 (1988) 122501.

[20] A. Winther and K. Alder, *Nucl. Phys. A* 319 (1979) 518.

[21] C. J. Joachain and C. Quigg, *Rev. Mod. Phys.* 46 (1974) 279.

[22] K. V. Shajesh, *Eikonal Approximation*, Study report, University of Oklahoma, USA (2004).

[23] M. Tanaka et al., *RCNP Annual Report* (1991) p. 215,
K. Takahisa et al., *RCNP Annual Report* (1994) p. 190,
H. Takahisa et al., *RCNP Annual Report* (1996) p. 172,
H. Tamura et al., *RCNP Annual Report* (1997) p. 289.

[24] K. Hatanaka, K. Takahise, H. Tamura, M. Sato and I. Muira, *Nucl. Instr. Meth. A* 384 (1997) 575.

[25] T. Shimoda, H. Miyatake and S. Morinobu, *Nucl. Instr. Meth. B* 70 (1992) 320.

[26] H. Sakai, H. Okamura, H. Otsu, T. Wakasa, S. Ishida, N. Sakamoto, T. Uesaka, Y. Satou, S. Fujita and K. Hatanaka, *Nucl. Instr. Meth. A* 369 (1996) 120.

[27] M. Fujiwara, H. Akimune, I. Daito, H. Fujimura, Y. Fujita, K. Hatanaka, H. Ikegami, I. Ka- tayama, K. Nagayama, N. Matsuoka, S. Morinobu, T. Noro, M. Yoshimura, K. Sakaguchi, Y. Sakemi, A. Tamii and M. Yosoi, *Nucl. Instr. Meth. A* 422 (1999) 484.

[28] N. Matsuoka, K. Hatanaka, S. Morinobu, T. Noro, A. Okihana and K. Sagara, *RCNP Annual Report* (1991) 186.

[29] T. Noro, Y. Mizuno, H. Togawa, S. Hirata, N. Matsuoka, O. Kamigaito, F. Hiei, Y. Sakemi, H. Akimune and T. Takahashi, *RCNP Annual Report* (1990) 217.

[30] M. Yosoi, H. Akimune, I. Daito, M. Fujiwara, S. Hirata, T. Inomata, O. Kamigaito, M. Kawabata, T. Noro, Y. Sakemi, T. Takahashi, A. Tamii, S. Toyama, A. Yamagoshi, M. Yoshimura and H. Sakaguchi, *Proc. of the 11 th Intern. Symp. on High Energy Spin Phys. AIP Conf. Proc.* 343 (1995) 157.

[31] M. W. McNaughton, B. E. Bonner, H. Ohnuma, O. B. Van Dijk, Sun Tsu-Hsun, C. L. Hollas, D. J. Cremans, K. H. McNaughton, P Riley, R. F. Rodebaugh, Shen-Wu Xu, S.E. Turpin, B. Aas and G.S. Weston, *Nucl. Instr. Meth. A* 241 (1985) 435.

[32] H. Fujita, Y. Fujita, G. P. Berg, A. D. Bacher, C. C. Foster, K. Hara, K. Hatanaka, T. Kawabata, T. Noro, H. Sakaguchi, Y. Shimbara, T. Shinada, E. J. Stephenson, H. Ueno and M. Yosoi, *Nucl. Instr. Meth. A* 484 (2002) 17.

[33] Y. Fujita, K. Hatanaka, G. P. Berg, K. Hosono, N. Matsuoka, S. Morinobu, T. Noro, M. Sato, K. Tamura and H. Ueno, *Nucl. Instr. Meth. B* 126 (1997) 274.

[34] A. Tamii, T. Adachia , J. Carter, M. Dozono, H. Fujita, Y. Fujita, K. Hatanaka, H. Hashimoto, T. Kaneda, M. Itoh, T. Kawabata, H. Matsubara, K. Nakanishi, P. von Neumann-Cosel, H. Okamura, A. Perez, I. Poltoratska, V. Ponomarev, L. Popescu, A. Richter, B. Rubio, H. Sakaguchi, Y. Sakemi, Y. Sasamoto, Y. Shimbara, Y. Shimizu, F.D. Smit, Y. Tameshige, M. Yosoi, J. Zenihiro and K. Zimmer, *Nucl. Instr. Meth. A* 788 (2007) 53c-60c.

[35] http://cern.ch/paw/,
http://cern.ch/cernlib/.

[36] M. Galassi, J. Davies, J. Theiler, B. Gough, B. Jungman, M. Booth and F. Rossi, *GNU Scientific Library Reference Manual*, 2nd ed. (Network Theory Ltd., Bristol, 2003) `http://www.gnu.org/software/gsl/`.

[37] H. Matsubara, *Study of M1 quenching in ^{28}Si by a (p,p') measurement at zero-degrees*, M.Sc. thesis, Osaka University, Japan (2006), unpublished.

[38] Computer program KINMAT, iThemba Laboratory for Accelerator Based Sciences, Faure, South Africa, unpublished.

[39] gnuplot, version 4.4 patchlevel 0
`http://www.gnuplot.info/`.

[40] `http://www.nndc.bnl.gov/ensdf/` (accessed: 01.08.2011).

[41] A. Tamii, *priv. communication* (2011).

[42] G. F. Bertsch and O. Scholten, *Phys. Rev. C* 25 (1982) 804-812.

[43] C. A. Bertulani, C. M. Campbell and T. Glasmacher, *Comp. Phys. Comm.* 152 (2003) 317-340.

[44] A. Shevchenko, J. Carter, R. W. Fearick, S. V. Förtsch, H. Fujita, Y. Fujita, Y. Kalmykov, D. Lacroix, J. J. Lawrie, P. von Neumann-Cosel, R. Neveling, V. Yu. Ponomarev, A. Richter, E. Sideras-Haddad, F. D. Smit, and J. Wambach, *Phys. Rev. Lett.* 93 (2004) 122501.

[45] Y. Kalmykov, T. Adachi, G. P. A. Berg, H. Fujita, K. Fujita, Y. Fujita, K. Hatanaka, J. Kamiya, K. Nakanishi, P. von Neumann-Cosel, V. Yu. Ponomarev, A. Richter, N. Sakamoto, Y. Sakemi, A. Shevchenko, Y. Shimbara, Y. Shimizu, F. D. Smit, T. Wakasa, J. Wambach and M. Yosoi, *Phys. Rev. Lett.* 96 (2006) 012502.

[46] S. Terashima, H. Sakaguchi, H. Takeda, T. Ishikawa, M. Itoh, T. Kawabata, T. Murakami, M. Uchida, Y. Yasuda, M. Yosoi, J. Zenihiro, H. P. Yoshida, T. Noro, T. Ishida, S. Asaji and T. Yonemura, *Phys. Rev. C* 77 (2008) 024317.

[47] J. Zenihiro, *Neutron density distributions of* ^{204,206,208}*Pb deduced via proton elastic scattering at* $E_p = 295$ *MeV*, Ph.D. thesis, Kyoto University, Japan (2011).

Danksagung

Hiermit möchte ich mich bei allen herzlich bedanken, die mich bei der Arbeit an meiner Bachelor-Thesis unterstützt haben.

Zunächst möchte ich mich bei Herr Prof. Dr. Peter von Neumann-Cosel für die freundliche Aufnahme in die Arbeitsgruppe sowie für die Möglichkeit, dieses spannende Gebiet der Physik im Rahmen der Bachelor-Thesis zu untersuchen, bedanken. Er hat meine Arbeit mit großem Interesse verfolgt und stand bei Fragen stets zur Verfügung. Weiterhin bin ich ihm dafür dankbar, dass ich an der Frühjahrestagung der DPG im März 2011 teilnehmen durfte.

Ganz besonders möchte ich mich bei Dr. Iryna Poltoratska, Anna Maria Krumbholz M.Sc. und Andreas Krugmann M.Sc. für die außerordentlich umfangreiche Betreuung bedanken. Sie waren immer offen für Fragen und Diskussionen und trugen durch ihre motivierende Art sowie konstruktive Kritik maßgeblich zum Gelingen dieser Arbeit bei. Hierbei möchte ich noch einmal Iryna hervorheben, die mich immer wieder engagiert unterstützt hat.

I am very grateful to Professor Dr. Atsushi Tamii for various fruitful discussions on his visit in August. I deeply appreciate his unresting help concerning the experiment and the data analysis.

Dr. Linda Schnorrenberger und Christopher Romig M.Sc. danke ich für die Bereitstellung der $^{144}\mathrm{Sm}(\gamma,\gamma')$ Daten.

Bei Johannes Simonis möchte ich mich für die Diskussion von zahlreichen Fragen und Problemen bedanken.

Außerdem danke ich allen Kollegen im Zimmer 22 und der gesamten Arbeitsgruppe für die gute Zusammenarbeit und das überaus positive Arbeitsklima.

Mein Dank gilt auch allen, welche Korrektur gelesen haben.

Schließlich möchte ich meiner Familie, meinen Freunden und Kommilitonen danken, die mich während des Studiums stets begleitet und unterstützt haben. Ein großer Dank geht an meine Freundin Bettina Bernhard, die mir vor allem in der abschließenden Phase so viel Geduld, Unterstützung und Verständnis entgegenbrachte.

Die vorliegende Arbeit wurde gefördert durch die DFG im Rahmen des Sonderforschungsbereich 634 und durch das Projekt NE 679/3-1.

Erklärung zur Eigenständigkeit

Hiermit versichere ich, Dirk Martin, die vorliegende Bachelor-Thesis ohne Hilfe Dritter und nur mit den angegebenen Quellen und Hilfsmitteln angefertigt zu haben. Alle Stellen, die aus Quellen entnommen wurden, sind als solche kenntlich gemacht worden. Diese Arbeit hat in gleicher oder ähnlicher Form noch keiner Prüfungsbehörde vorgelegen.

Darmstadt, den 4. Oktober 2011

_____

(Dirk Martin)